IDENTIFIED CHARGED HADRON PRODUCTION IN Au-^{3}He COLLISIONS AT $\sqrt{s_{NN}} = 200$ GeV

A thesis Submitted
in Partial Fulfilment of the Requirements
for the Degree of

MASTER OF SCIENCE

by

TANMAY PANI

to the

School of Physical Sciences

National Institute of Science Education and Research

Bhubaneswar

7th June 2020

DECLARATION

I hereby declare that I am the sole author of this thesis in partial fulfillment of the requirements for a postgraduate degree from National Institute of Science Education and Research (NISER). I authorize NISER to lend this thesis to other institutions or individuals for the purpose of scholarly research.

Signature of the Student
Date:

The thesis work reported in the thesis entitled .....
was carried out under my supervision, in the school of .....
at NISER, Bhubaneswar, India.

Signature of the thesis supervisor
School:
Date:

ACKNOWLEDGEMENTS

I would like to give my most sincere gratitude to my thesis supervisor, Prof. Bedangadas Mohanty for giving me a chance to do this project. He has been a constant source of inspiration since the day I joined NISER, and will remain so long after I graduate. Whatever I am, and whatever I will be, is made possible by the grace and goodwill of Prof. Mohanty. I shall also thank Ashish Pandav, Debashis Mallick, Dr. Ranbir Singh and Dr. Rihan Haque for significantly guiding me through the project. I also extend my gratitude to Dr. Md Nasim for helping me with the initial codes and Dr. Lokesh Kumar and Dr. Debadeepti Mishra for helping me with the spectra analysis. I would like thank all the members of our group, who were kind enough to interact with me and helped me in any form and for organizing many group events which kept my spirits up. Lastly, I thank my family for standing by me and supporting me through everything.

ABSTRACT

In this thesis, we have done extraction and study of $\pi^{\pm}$, $K^{\pm}$ and $p(\bar{p})$ from STAR and AMPT data for Au-^{3}He collisions at $\sqrt{s_{NN}} = 200$ GeV. We started with event and track QA selection followed by centrality determination for the 200 GeV Au-^{3}He events. Then we proceed to extracting raw yeilds using dE/dx method in STAR-TPC and m^2 fitting in TOF detector. Observables like average transverse momentum ($\langle p_T \rangle$), particle yields (dN/dy) and kinetic freeze-out properties are extracted from AMPT-SM data. Kinetic freezeout properties are extracted using hydrodynamics-motivated blast-wave model fits to the data .

In the appendices, we have discussed the theoretical description of the ^{3}He nucleus using Green's Function Monte Carlo (GFMC) Method. We have compared AMPT simulations, with and without modified ^{3}He distribution. We see that the Pearson correlator and eccentricities are lower when we use modified ^{3}He nuclear profile.

Future plans are also discussed.

Contents

List of Figures

List of Tables

Chapter 1

Introduction

1.1 The Standard Model

The Standard model(SM) is the theory of fundamental constituents of matter and how they interact[1]. The model consists of three types of fundamental particles, Quarks, Leptons and Gauge bosons. Quarks and Leptons are fermions, and any interaction between them is mediated through the Gauge Bosons. There are a total of six different gauge bosons, photons (γ), gluons (g), $W^{\pm}$, Z^0 and the Higgs boson (H). The standard model bosons describe three out of four fundamental forces, the electromagnetic, weak and strong forces. There are three generations of leptons in the SM : The electron(e) and electron neutrino(ν_e), the muon(μ) and muon neutrino(ν_μ), and the tau(τ) and tau neutrino(ν_τ). The leptons can interact only via the electromagnetic and the weak interaction. SM also has six quarks which are again divided into three generations: The up (u) and down (d) quarks, the charm (c) and strange (s) quarks, and the top (t) and bottom (b) quarks. The standard model particles get their mass by interacting with the Higgs boson.

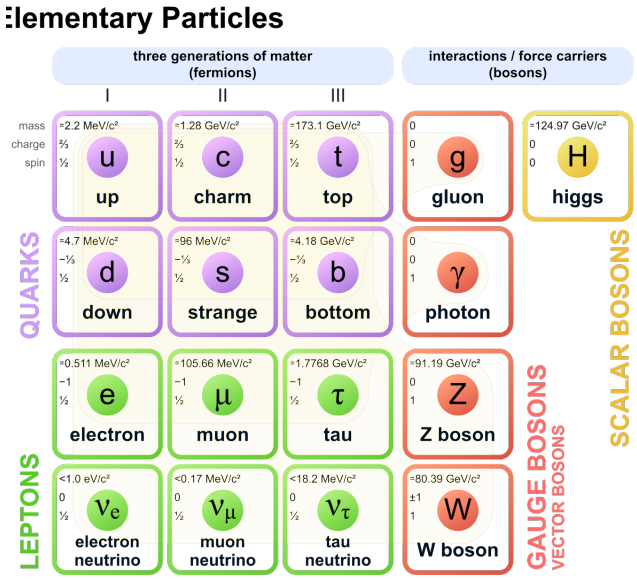

Figure 1.1: A chart showing various SM particles[2].

1.2 Quantum Chromodynamics

The theory of strong interactions is called Quantum Chromodynamics (QCD). The basic fundamental particles involved are quarks, which are fermions with spin 1/2, and the gluons which are bosons with spin 1. We denote the quark field by q_f , with f being the flavor. The quark flavors are q_f : u, d, s, c, b, t corresponds to nomenclature up, down, strange, charm, bottom, and top quarks. The quarks can also have three color states. The strong interaction field or the gluon field is given by A^a_μ with the index a denoting the 8 possible color states of gluons. The interaction of quarks with gluons can be hence written as,

$$V_{qg} = \sum_f \overline{q}_f \gamma^\mu g_s A_\mu q_f$$
$$A_\mu = \sum_1 A^a_\mu \lambda^a / 2 \tag{1.1}$$

where the quanta of A_μ are gluons, γ_μ are the Dirac matrices and g_s is the strong interaction coupling constant. The λ_a are the SU(3) color matrices, with

$$\lambda^a\lambda^b - \lambda^b\lambda^a = i2\sum_{c=1}^{8} f^{abc}\lambda_c \tag{1.2}$$

with f^{abc} the SU(3) structure constants.

The two important consequences of strong interaction are confinement and asymptotic freedom. These phenomena can be understood by looking at the expression of coupling strength (α_s) of the strong interaction,

$$\alpha_s(Q^2) = \frac{12\pi}{(11n - 2f)\ln(|Q^2|/\Lambda^2)}. \tag{1.3}$$

Where, Q^2 is the momentum transfer or the energy scale, n is the number of colors and f is the number of flavors. The Λ vakue lies in the range $100\text{MeV} < \Lambda < 500\text{MeV}$.

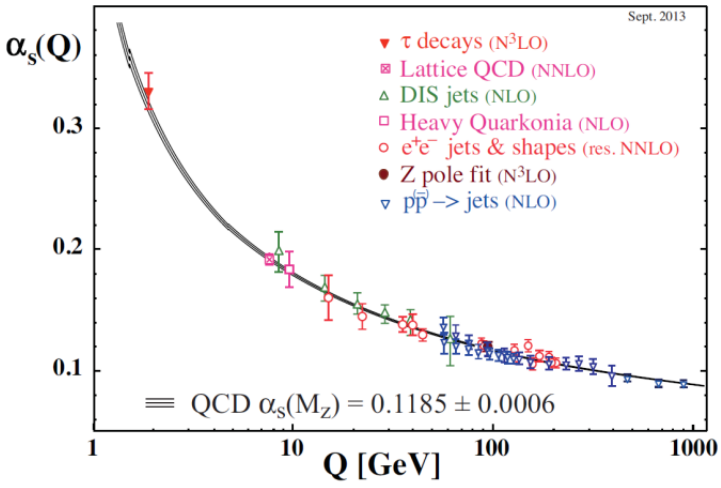

Figure 1.2: Various measurements on the strong coupling constant, α_s as function of energy scale Q.[3]

For small momentum transfer (energy scales) or at larger distance scales, the value of α_s is high and increases as the distance between the quarks increases. This property is known as confinement[4] and is responsible for binding of quarks inside the

hadrons. On the other hand, when momentum transfers or energy scales are large i.e., distance between the quarks are very small, the coupling between quarks becomes very small and quarks behaves like free particles. This is known as Asymptotic freedom[4]. Confinement and Asymptotic freedom lead to the formation of a state with deconfined quarks and gluons called Quark-Gluon Plasma (QGP). The details of this exotic state of matter will be discussed in subsequent sections.

1.3 Quark-Gluon Plasma

At low density, a particular quark is confined to a hadron and has a "hadronic identity". However, at high enough density, when the hadrons starts to interpenetrate each other, a particular quark will not able to identify which other quark belonged to the same hadron. Hence the quarks lose their hadronic identity. Similar phenomena can happen at high temperature. As we increase the temperature of nuclear matter, more matter (hadrons) is produced and this leads to an increase in density. Thus, at high temperature and high density, the relevant degree of freedom would change from hadrons to quarks and gluons (partons). As discussed in the previous section (1.2), at short enough distances, or at large enough energy scales, quarks and gluons become free and such dense nuclear matter of free quarks is known as the Quark-Gluon Plasma (QGP)[5]. Formally, we define QGP as a thermalised, or near to thermalised state of quarks and gluons, where quarks and gluons are free to move over a nuclear volume rather than a nucleonic volume[6].

Since quarks are confined within the hadrons at low density or low temperature and are deconfined at high density or at high temperature, we can think about a confinement-deconfinement phase transition. Lattice QCD calculations also theorize the presence of two phases in the high temperature QCD, which are identified with

the hadronic and partonic phase, respectively.

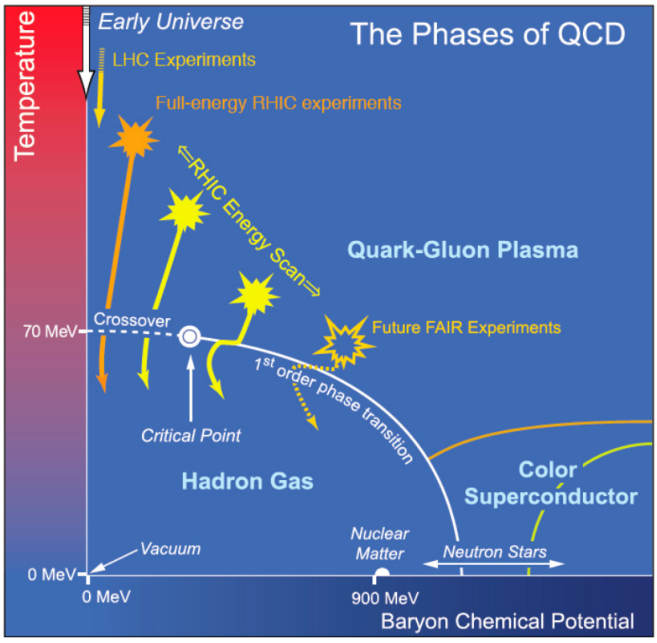

Figure 1.3: Schematic QCD phase diagram for nuclear matter[8]. The solid lines show the phase boundaries for the indicated phases. The solid circle depicts the critical point[9].

At a critical temperature $T_c \approx 155 - 175$ MeV (at chemical potential $\mu_B \approx 0$), we find a sharp increase in energy density. This indicates sudden change in the degrees of freedom of the system i.e. de-confinement of hadrons into partons. A state of de-confined quarks and gluons is expected to be present at very high T and low μ_B , while quarks and gluons are known to be confined inside hadrons at low T and low μ_B. QCD calculations suggest a colour super-conducting phase[7] at low T and high μ_B quarks.

1.4 Relativistic Heavy Ion Collisions

To study QGP, we first need to create it. Colliding two heavy nuclei (Heavy atoms with all their electrons stripped off) like, Au, Pb, U, Cu, etc. at relativistic speeds

(also called Relativistic Heavy Ion Collisions) using large machines called Ion/Hadron colliders is a convenient way to create QGP and study it in a controlled laboratory setting. The Relativistic Heavy Ion Collider (RHIC) in BNL, US and the Large Hadron Collider (LHC) in CERN, Geneva have acomplished the creation of QGP. The next two sections will be discussing the space-time evolution and kinematics of Heavy Ion Collisions.

1.4.1 Space-time evolution

As the two colliding nuclei travel towards each at relativistic speeds, they undergo Lorentz contraction along the beam direction and appear as two flat pancakes to an observer at rest at their center of mass (center of mass frame). At time $t = 0$, the two nuclei hit each other, the partons in the overlapped region start interacting inelastically. These inelastic interactions lead to the loss of kinetic energy. The lost kinetic energy creates matter (particles) in the vicinity of the collision which is often called as the fireball. If the fireball is hot enough, the QGP is formed. As the fireball expands and cools to a critical temperature T_c, quarks and gluons will coalesce to form a hadron gas. As the hadron gas expands, inelastic interactions will eventually stop at the chemical freeze-out, with a temperature T_{ch}. The chemical composition will not change further. After further expansion, elastic interactions will stop at kinetic freeze-out, with an associated temperature T_{fo} or T_{kin}.

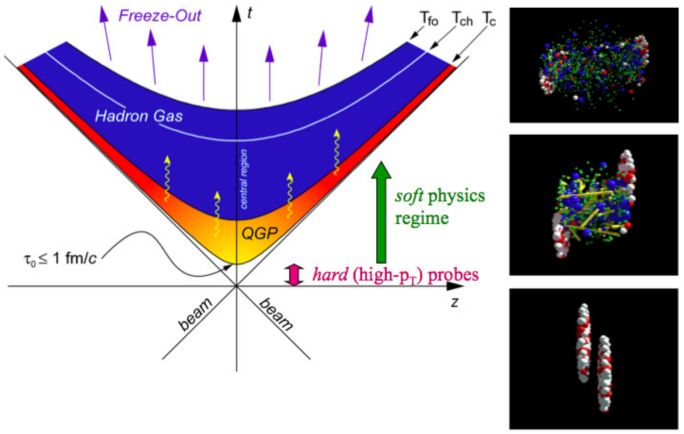

Figure 1.4: The space-time evolution of a heavy-ion collision [11].

1.4.2 Kinematics

At most collider experiments like RHIC or LHC, the coordinate system used is chosen such that the z-axis is parallel to the collision or beam axis. The interaction point (IP) is expected to be at $(0, 0, 0)$. The beams are focused such that collisions take place around this point. However, collisions do not always happen exactly at the IP. Thus the collision point also has to be reconstructed, this is called the primary vertex.

Below, we describe some of the important kinematic variables which will be used throughout this report[10].

Transverse Momentum

The total momentum is split into two components, one parallel to the collision axis called the transverse momentum (p_T), and one parallel, called longitudinal momentum (p_z). Transverse momentum is defined as:

$$p_T = \sqrt{p_x^2 + p_y^2} \tag{1.4}$$

where p_x and p_y are the x and y components of total momentum (p). The transverse momentum is Lorentz invariant.

Rapidity

Since in relativistic limit, p_z is not additive, we use another variable called rapidity, given by,

$$y = \frac{1}{2} \ln \left(\frac{E + p_z}{E - p_z} \right) \tag{1.5}$$

Pseudo-rapidity

Sometimes, measuring both energy and momentum may not be straightforward or possible. This mainly happens in case of unidentified particles. So experimentalists often use the pseudo-rapidity (η) variable for such cases:

$$\eta = -\ln[\tan(\theta/2)] \tag{1.6}$$

Where, $\theta = \tan^{-1}(p_T/p_z)$.

In terms of rapidity,

$$\eta = \frac{1}{2} \ln \frac{\sqrt{m_T^2 \cosh^2 y - m^2} + m_T \sinh y}{\sqrt{m_T^2 \cosh^2 y - m^2} - m_T \sinh y}. \tag{1.7}$$

Azimuthal angle

Angle made by transverse momentum vector with x-axis.

$$\phi = \tan^{-1} \frac{p_y}{p_x} \tag{1.8}$$

These variables are calculated first in a track loop and used in analysis.

Multiplicity

The number of particles that are produced in an event (one collision) is called multiplicity. Generally, we only count the charged particles while calculating multiplicity. Therefore, charged particle multiplicity would be a more accurate name of this variable.

Invariant distribution

The quantity $E\frac{d^3\sigma}{dp^3}$ is called invariant cross section as the quantity $\frac{d^3p}{E}$ is invariant under Lorentz transformations. In experiments, we measure the invariant cross section by using the equivalent expression,

$$E\frac{d^3\sigma}{dp^3} = \frac{1}{L_{int}}E\frac{d^3N}{dp^3} = \frac{1}{L_{int}2\pi}\frac{d^2N}{p_T dp_T dy} \tag{1.9}$$

where σ is the cross section of the collision, E is the energy of the particle and L_{int} is the integrated luminosity. Luminosity is the number of particles per unit area per unit time times the opacity of the target. Often, the total number of events (N_{evts}) is taken as a proxy instead of L_{int}.

Collision Centrality

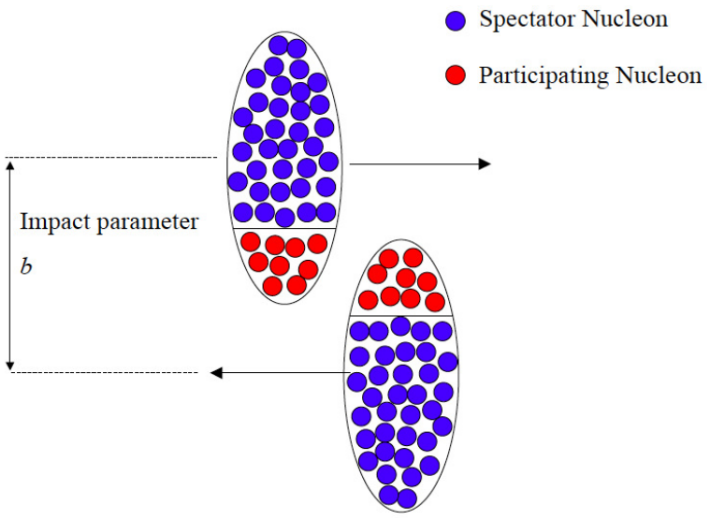

Figure 1.5: A schematic diagram of a HI collision event.

The component of the distance between the centre of one nucleus and that of the other perpendicular to the collision axis, is called the impact parameter (b). It is a measure of overlap of the two colliding nuclei. The nucleons inside the overlap region are called participant nucleons. The central collisions are the ones having a small impact parameter and a large number of participating nucleons, peripheral collisions are defined as having a large impact parameter and a small number of participating nucleons. As the impact parameter cannot be directly measured experimentally, the produced charged particle multiplicity is often used to characterize centrality. This can be done by assuming that multiplicity is a monotonic function of the impact parameter. This would lead to higher values of multiplicity corresponding to central collisions and lower values to peripheral collisions. The details of centrality determination technique will be discussed in chapter 3.

1.5 Motivation

In a heavy-ion collision experiments to study QGP and the QCD phase diagram, after the collision happens, a QGP fireball is formed and as it expands and cools, it transitions into a hadron gas and after it undergoes chemical and then kinetic freeze-out, only $\pi^{\pm}$, $K^{\pm}$ and $p(\bar{p})$ manage to survive long enough to reach the detector. The higher resonances decay into one of these hadrons. As these hadrons move through the detector medium, they ionize the medium in a particular way, and produce signals characteristic to their charge and mass. By analyzing these signals, we can identify these particles. Hence, $\pi^{\pm}$, $K^{\pm}$ and $p(\bar{p})$ are known as identified charged hadrons. The motivation of this thesis is to study the transverse momentum distribution of these identified hadrons and make some estimations of some bulk properties of the QGP fireball.

The thesis is organized as follows. After the introduction (chapter 1), we have discussed about the Solenoid Tracker at RHIC (STAR) experiment in chapeter 2. In chapter 3, we present event selection and centrality determination of the events in STAR Au-^{3}He collisions at 200GeV. In chapter 4, we discuss particle identification from the Time Projection Chamber (TPC) and Time of Flight (TOF) detectors. We also do extraction of raw π, K, p spectra. In chapter 5, we get π, K, p spectra from data generated from A Multi Phase Transport (AMPT) model and extract some bulk properties like mean p_T ($\langle p_T \rangle$), particle yeild (dN/dy) and kinetic freezeout parameters fitting the AMPT spectra to the hydrodynamics motivated Blast-wave model. We have also discussed summary and outlook at the end of each chapter.

Chapter 2

Solenoid Tracker At RHIC (STAR)

STAR is an experiment at the Relativistic Heavy Ion Collider (RHIC) in Brookhaven National Laboratory, United States. STAR's major physics goal is to study the formation and characteristics of the quark-gluon plasma (QGP) state. Detecting and understanding the QGP state would give us valueable insights into the Universe moments after the Big Bang, where the symmetries (and lack thereof) of our surroundings were put into action.

Due to the complexity of the system formed in the high-energy heavy ion collisions and the relatively unexplored landscape of physics at high energy scales, to make solid inferences about the QGP, STAR makes use of a variety of simultaneous analyses. Theresfore, STAR takes help from many types of detectors, each of which specialize in detection and tracking of certain types of particles. These detectors work together in an advanced data acquisition and subsequent physics analysis that allows one to arrive at some conclusions about the collision.

STAR is composed of 67 institutions from 13 countries, with a total of 692 collaborators.

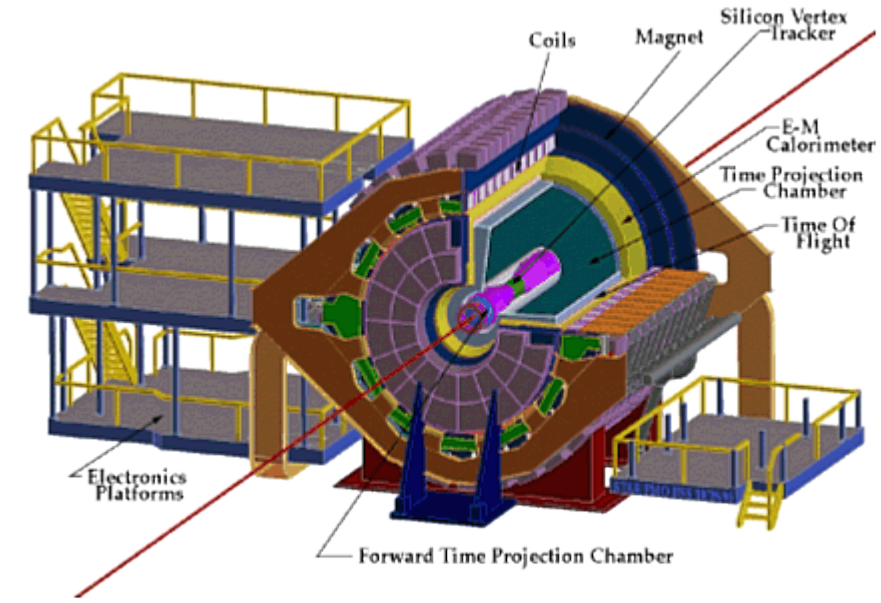

Figure 2.1: Schematic representation of STAR experimental setup [12].

2.1 Time projection chamber (TPC)

The TPC is the primary tracking device of STAR. It helps identify charged particles from their ionization energy loss (dE/dx) as they travel through the gas volume of the TPC. It has full azimuthal coverage and a pseudorapidity acceptance of $|\eta| < 1.8$. It is 4.2m long, 4m in diameter, filled with P10 gas (10% Ar and 10% CH_4) and divided into two drift chambers by central membrane, with a uniform electric field of 135 V/m. A uniform magnetic field surrounds it in the z direction. Depending on their charge and mass, the trajectory of the particles traversing the TPC will curve one way or the other in xy plane due to interactions with the magnetic field, and leave a trail ioinized atoms in the active detector volume.

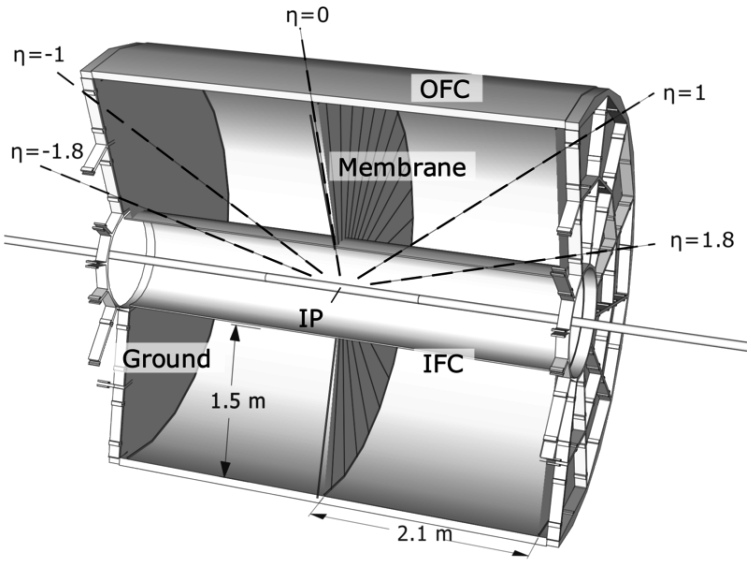

Figure 2.2: A schematic diagram of TPC [12].

2.2 Time of flight (TOF)

The STAR Time-of-Flight (TOF)[13] system extends the experiment's particle identification capabilities to high p_T region. It has a highly segmented cylindrical detector which immediately surrounds the TPC and is arranged in 120 trays. Each individual tray has the dimensions 2.4m $\times$ 21.3cm $\times$ $\times$8.5cm. Each tray has an azimuthal coverage of 6 degrees around the TPC. In each tray, there are 32 Multigap Resistive Plate Chamber (MRPC)[15] modules which are placed along the beam (z) direction. The MRPC is a stack of parallely arranged resistive plates. create A series of gas gaps is created by the intermediate plates. The outer surfaces of the two outer plates have electrodes attached. Applying a high voltage across these external electrodes generates a strong electric field in each subgap. A charged particle generates avalanches in the gas gaps as it goes through the chamber. The plates are transparent to signal induced by avalanches as they are resistive, thus a signal induced in the pickup pad is the sum of signals from all the gas gaps. TOF system consists of TOF trays and

Vertex Position Detectors (VPDs)[14]. The stop time of every track is provided by TOF trays. Start time of the event is provided by VPD. The difference between these two times is called the time of flight (τ) of the track. TOF has a time resolution of $\approx$ 80 to 100 ps. Time of flight of each track relates to the mass of that track using the expressions,

$$\begin{aligned} \beta &= L/c\tau \\ \gamma &= 1/\sqrt{1-\beta^2} \\ m &= \mathrm{p}/\gamma\beta\mathrm{c} \end{aligned} \tag{2.1}$$

where L is the length of the path travelled by the particle (path-length), c is the speed of light, m is the mass of the particle and p is the momentum measured by the TPC. Using information from TOF we can separate π/K and p/K upto $p \approx 1.6$ and 3.0 GeV/c, respectively.

2.3 Trigger detectors

The four major trigger detectors in STAR are the Zero Degree Calorimeters (ZDCs), Beam Beam Counters (BBCs), the Vertex Position Detectors (VPDs)[14], and the Electromagnetic Calorimeter (EMC). The purpose of the STAR trigger is to instruct the slower detector subsystems which have different readout speeds, on when to record data.

The two ZDCs are positioned at $\pm$18.25 metres along the collision axis. The ZDCs are hadronic calorimeters which measure the energy from the remaining neutrons from the heavy-ion collisions after the event in a very small (nearly zero) solid angle($\theta < 2$ mrad). The energy deposited by the neutrons can be related to the multiplicity. For a minimal bias trigger, we need a coincidence of the signal between the two ZDCs with a summed signal greater than $\approx$ 40% of a single neutron signal.

The BBC has a hexagonal scintillator array structure, located on each side of the collision point. It has full azimuthal coverage and an η coverage of $2.1 < |\eta| < 5.0$. It

is placed around the beam pipe at a distance of 3.7 m from the collision point. For a minimal bias trigger, we need a coincidence of the signal between the two BBC. The time difference between the two counters gives us information on the primary vertex position. BBC coincidences are also used to reject beam gas events. In addition, the small tiles of BBC are also used to reconstruct the first order event plane for flow analysis.

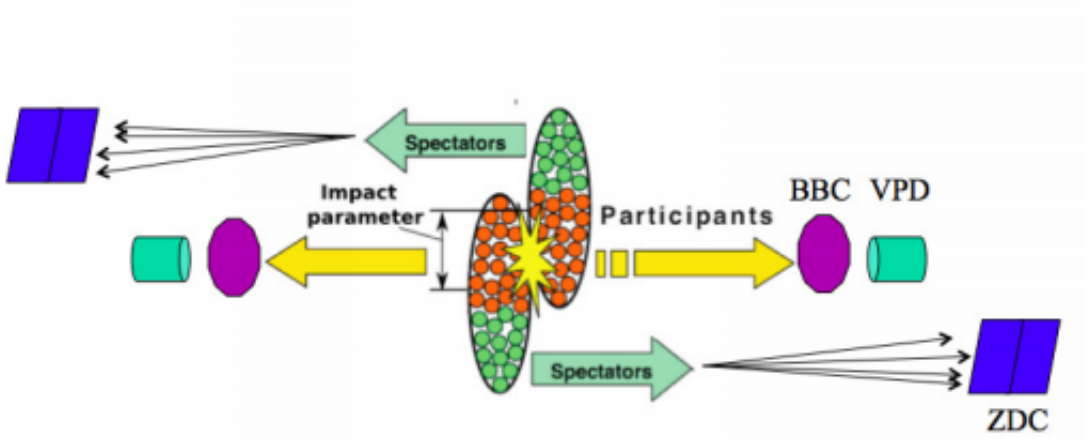

Figure 2.3: A schematic figure of a nucleus-nucleus collision and STAR trigger systems [11].

Each VPD comprises of 19 lead converters and plastic scintillators with photomultiplier tube readout that are placed very close to the beam pipe on each side of the STAR detector setup. Each VPD is around 5.7 m from the collision point and has a pseudo-rapidity coverage of $4.24 < |\eta| < 5.1$. For a minimal-bias (MB) trigger using VPD, we need a coincidence of the signals between the east and west VPD detectors. The VPD can also provide the details about the z component of the vertex. The timing resolution of VPD is superior to that of BBC.

The Electromagnetic Calorimeters (EMC) are used to select events with rare probes such as high energy γ and π^0 particles, or electrons from J/ψ decays.

Chapter 3

Centrality Determination of Au-^{3}He collisions

Collisions or events are classified into centrality classes where, the most central class consists of events with the lowest impact parameters, which leads to highest multiplicities. Thus, experimentally, when the total integral of the multiplicity distribution is known, we define the centrality classes by binning the multiplicity distribution based upon the percentile of the total integral.

In this analysis, we have used the event variable called RefMult or Reference multiplicity, which is the number of charged particles in an event with $|\eta| < 1$.

3.1 Data set and Event selection

The data analyzed in this work were recorded by the STAR experiment at the Relativistic Heavy Ion Collider (RHIC) during the year 2014, at the center of mass energy $\sqrt{s_{NN}} = 200$ GeV for Au+^{3}He collisions. The trigger taken for this analysis is ZDCE (Id: 460001)

3.1.1 Event selection

We select the minimum bias triggered events with a primary collision vertex position along the longitudinal beam direction (V_z) obeying $V_z < 30cm$. In addition to this, a radial vertex cut for the transverse position of the primary vertex ($V_r < 2$ cm) from the center of the interaction point is applied for selecting good events. Also, another cut was applied on $|\Delta V_z| = |V_z - V_z^{VPD}|$, it is the absolute difference between

the z-components of the collision veritices as measured by TPC and VPD. $|\Delta V_z|$ was restricted to 3cm. This criteria is set to remove pile-up events.

3.1.2 Bad runs removal

Run numbers (events taken during a time period) for which an observable shows too much fluctuation is designated as a "bad run". We look for bad runs by studying the variation of average values of various observables with run number. After that, we check, for which run numbers the average of the observable in that run number bin deviates by more than 3σ from the total average of the observable, sigma being the standard deviation of the observables over the run numbers. Those are the bad-runs which are rejected.

We have used 5 observables for this purpose, RefMult, DCA, transverse momentum (p_{T}), pseudorapidity and Azimuthal angle (ϕ).

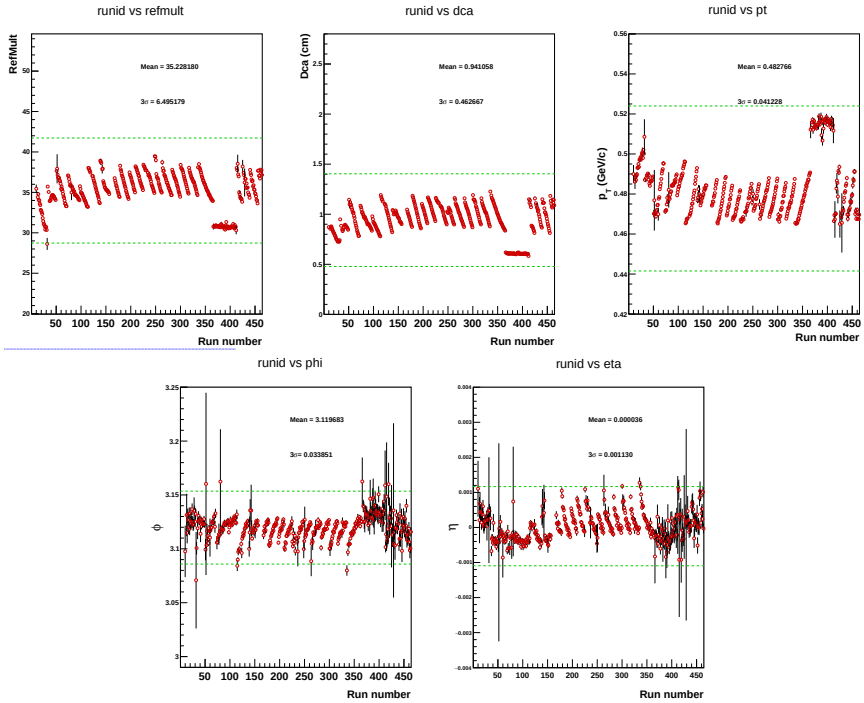

Figure 3.1: Average values of the observables plotted against their run number. The green lines denote the 3σ limit.

To summarise,

- **TriggerID:** 460001
- **Trigger label:** ZDCE
- **Total events for the trigger ID:** 300 million
- $|V_z| < 30$ cm
- $|V_r| = \sqrt{V_x^2 + V_y^2} < 2$ cm
- $|\Delta V_z| = |V_z - V_z^{VPD}| < 3$ cm
- **Total events after cuts, badrun rejections:** 52 million

3.1.3 Luminosity correction

We need to correct for dependence of refmult on beam luminosity. Therefore, we remove the dependence of RefMult on ZDC coincidence rate (used to calculate luminosity), by fitting a Refmult vs ZDC coincidence rate profile histogram with a linear function. Then we remove the dependence by multiplying Refmult by an appropriate factor in each event. If the fit function used of $p_0 + p_1 x$, then in every event, Refmult will be scaled by a factor ζ,

$$\zeta = \frac{p_0}{p_0 + p_1 \times \text{ZDCCoincidenceRate}} \tag{3.1}$$

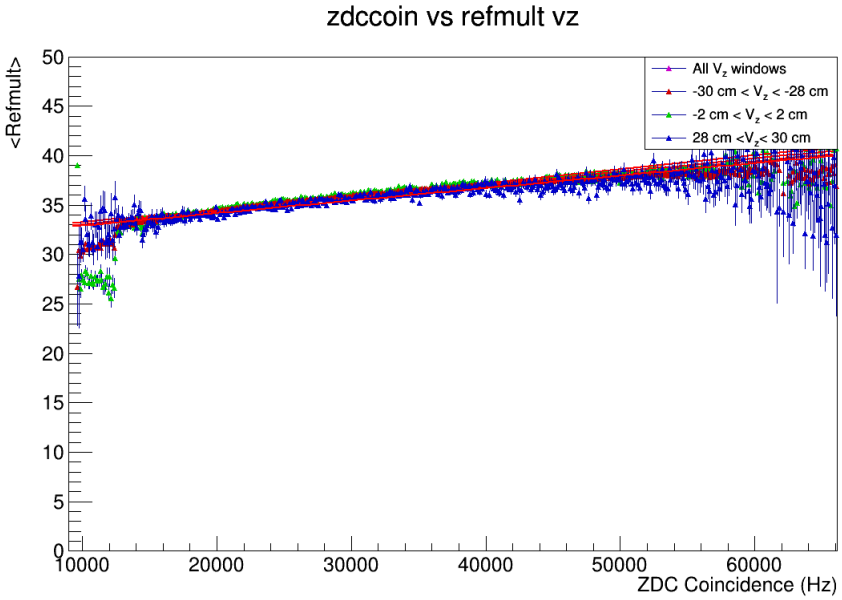

Figure 3.2: The linear fitting done in different V_z windows.

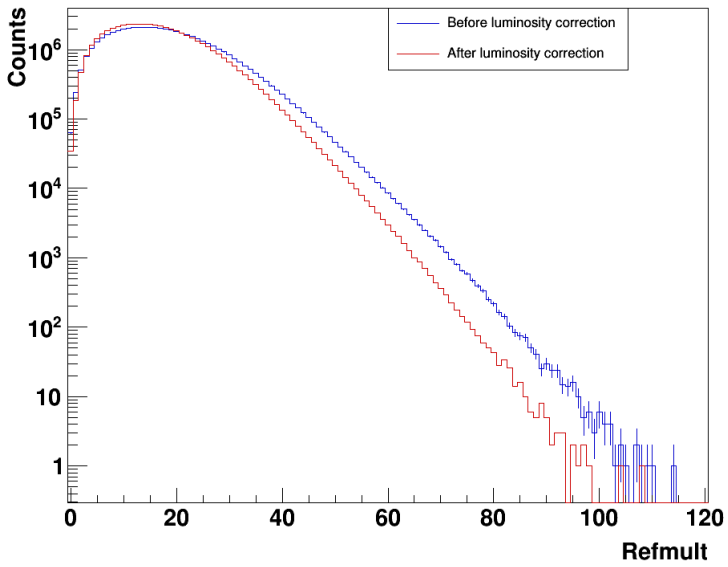

Figure 3.3: Comparision between the refmult distributions before(blue) and after(red) luminosity correction.

3.2 Glauber Monte Carlo Model

Glauber models are useful in calculating the quantities related to the initial state geometries of heavy ion collisions, like impact parameter(b), number of participating nucleons(N_{part}) and initial eccentricity(ϵ).

There are two main types of Glauber models. In the optical Glauber calculations, a smooth, spherically symmetric matter density is assumed, with the matter distribution in the radial direction being described by a Fermi distribution. In the Monte Carlo (MC) based models, individual nucleons are stochastically generated event-by-event and collision properties are multiple event averages.

For the purposes of this project, we have used the MC Glauber calculation implemented by PHOBOS.[22][23]

3.2.1 Inputs to the model

Nuclear density profile

The probability distributions of the nuclei are taken to be spherically symmetric. The radial distribution function is modeled after nuclear charge densities extracted from low-energy electron scattering experiments. The nuclear charge density is usually given by a three parameter Fermi distribution[22].

$$\rho(r) = \rho_0 \frac{1 + w(r/R)^2}{1 + \exp(\frac{r-R}{a})} \tag{3.2}$$

Where, ρ_0 is the nucleon density, R is the nuclear radius, a is the skin depth and w corresponds to small deviations from a spherical shape. This is the case for Au nucleus.

However, other modified distributions are used for deformed nuclei like U, Cu,

etc. These are of the form,

$$\rho(x,y,z) = \rho_0 \frac{1}{1+\exp\frac{(r-R(1+\beta_2 Y_{20}+\beta_4 Y_{00}))}{a}} \tag{3.3}$$

Where, $Y_{40} = \frac{3}{16\sqrt{\pi}}(35\cos^4(\theta) - 30\cos^2(\theta) + 3)$, $Y_{20} = \sqrt{\frac{5}{16\pi}}(3\cos^2(\theta) - 1)$. $\beta_{1,2}$ are the deformation parameters.

For ^{3}H and ^{3}He, the configurations of the three nucleons were computed and stored in a data file from Greens function MC (GFMC) calculations using the AV18 + UIX model interactions, which accurately sample the position of the three nucleons[23][18]. We will be discussing about this in the appendix.

Inelastic nucleon-nucleon cross-section

The next step is to simulate a nucleus-nucleus collision. The impact parameter b is randomly sampled from a geometrical distribution dP/db vs b up to a maximum $b_{max} \approxeq$ 20fm, which is large enough to simulate collisions until the interaction probability becomes negligible. The nucleus-nucleus collisions are seen as a bunch of independent nucleon-nucleon collisions, where the nucleons travel in a straight line and the same inelastic nucleon-nucleon cross section is used for all successive collisions (inelastic interactions between two colliding nuclei is independent of the preceding collisions). If the perpendicular distance between centers of the two nucleons coming from opposite directions (d) is less than the distance corresponding to the inelastic nucleon-nucleon cross section ($\sigma_{NN}^{\text{inel}}$), ($d < \sqrt{\sigma_{NN}^{\text{inel}}/\pi}$) then, the two nucleons from different nuclei are taken to be colliding.

The value of the cross-section $\sigma_{NN}^{\text{inel}}$ is typically estimated by interpolation of pp data at different center of mass energies and from cosmic rays, and subtracting the elastic scattering cross section from the total cross section. [17] [22]

In an event, the number of collisions N_{coll} is the number of binary nucleon collisions

$\sqrt{s_{NN}}$ (GeV/c)	$\sigma_{NN}^{\text{inel}}$(mb)
27	31.94
39	30.98
62.4	31.55
200	42
2760	64
5500	72

Table 3.1: Experimental values of $\sigma_{NN}^{\text{inel}}$ for given center of mass energies[17] [22].

and the number of participants N_{part} is the number of nucleons that experience at least one collision.

3.2.2 The NBD-Glauber fit to the multiplicity distribution

To reproduce the experimental multiplicity distribution, the Glauber Monte Carlo is coupled to a particle production model, based on a Negative Binomial Distribution (NBD). NBD is used in this way because it accurately describes the charged particle multiplicity in minimum bias pp collisions at high energy over a wide rapidity range.[25][26]

To apply this model to any collision with a given N_{part} and N_{coll} value we define a source, which independently emmits particles. The number of sources N_{source} is given by a two-component model, which decomposes the nucleus-nucleus collisions into soft interactions which produce particles with an average multiplicity proportional to N_{part} and hard interactions, where the soft interactions , probability of whose occurence is proportional to N_{coll}.[27]

The steps taken from here on are given below[24]:

- The number of independently emitting source particles are given by the Two component model:

$$N_{\text{source}} = \frac{(1-x)}{2} N_{\text{part}} + x N_{\text{coll}} \tag{3.4}$$

Where, x is the hard interaction fraction.

- We obtain the number of particles produced from each interaction using the Negative Binomial Distribution (NBD):

$$P(\mu; n_{\rm pp}, k) = \frac{\Gamma(\mu + k)}{\Gamma(\mu + 1)\Gamma(k)} \left(\frac{n_{\rm pp}}{k}\right)^{\mu} \left(1 + \frac{n_{\rm pp}}{k}\right)^{-(\mu+k)} \tag{3.5}$$

  Where, P is the probabitity of measuring μ particles per source particle. $n_{\rm pp}$ is the mean and k is the width of the NBD.

- For every Glauber MC event, the NBD is sampled N_{source} times and summed over to get the multiplicity for the Glauber MC event.

- Histograms are drawn of the Glauber MC events and compared with data

- The best fit is chosen by using χ^2 minimisation.

Here, the free parameters are x (from the two component model) and $n_{\rm pp}$ and k from NBD. We take many cases of ($n_{\rm pp}$, k, x) and for each triplet we generate a glauber multiplicity distribution. Then we calculate the χ^2/NDF by comparing the glauber distribution with our data Refmult histogram. The minimization of χ^2/NDF is shown in Fig. 3.4.

Best fit was obtained for $n_{pp} = 4.34$, $k = 2.98$, $x = 0.13$. .

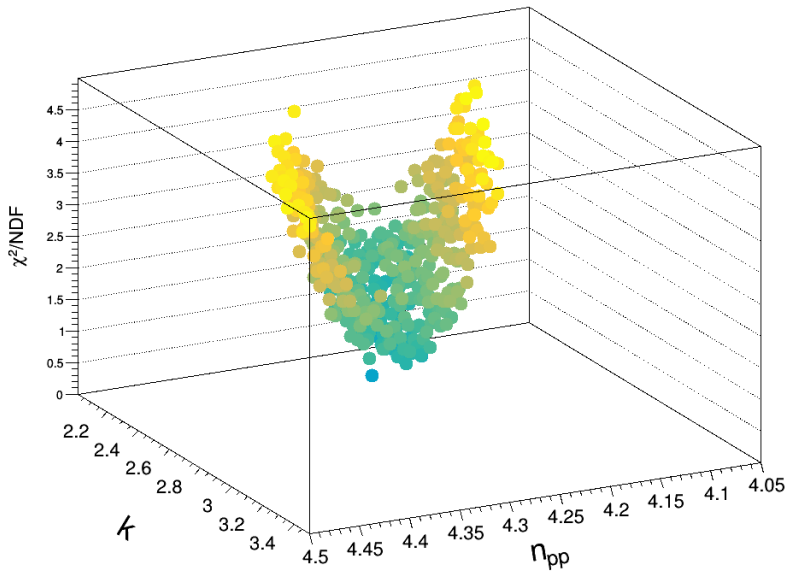

Figure 3.4: Plot showing variation of χ^2/NDF in neighbourhood of the obtained minima.

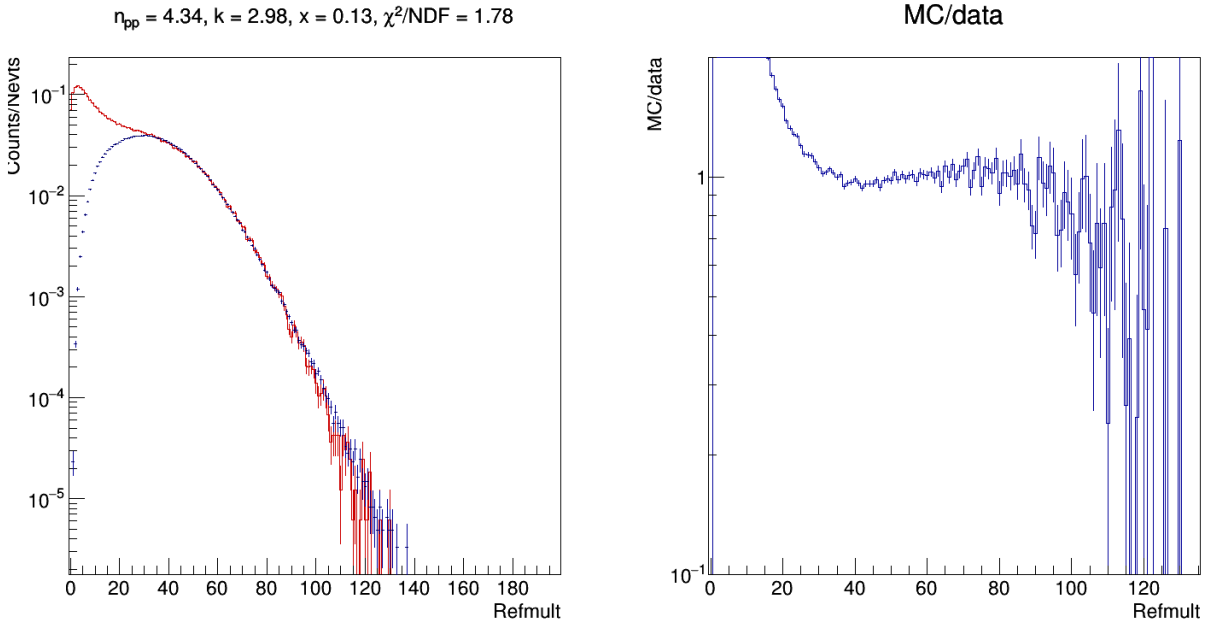

Figure 3.5: (Left) The best fit of Glauber-NBD histogram(red) with data multiplicity distribution (blue). (Right) The ratio of MC and data events in each Refmult bin.

The refmult ranges obtained for the 9 centrality classes are given below:

Centrality (%)	Refmult range
0 - 5	≥ 59
5 - 10	< 59 and ≥ 50
10 - 20	< 50 and ≥ 40
20 - 30	< 40 and ≥ 31
30 - 40	< 31 and ≥ 25
40 - 50	< 25 and ≥ 18
50 - 60	< 18 and ≥ 13
60 - 70	< 13 and ≥ 9
70 - 80	< 9 and ≥ 6

Table 3.2: Cuts for selecting different centrality classes.

Chapter 4

Particle production in Au-^{3}He collisions

4.1 Introduction and Data set

Exploring the QCD phase diagram and subsequently searching for the QCD critical point is one of the major tasks of relativistic heavy-ion collision (HIC) experiments. Studying the bulk properties of the fireball formed in high-energy HICs gives us useful insight on evolution of the system and on the particle production mechanism. As the fireball formed in high-energy HIC experiments evolves with time, two sequential freeze-out scenarios are observed, those are chemical freeze-out and kinetic freeze-out. At chemical freeze-out, the inelastic interactions among the particles cease fixing the particle yields. This surface is defined by the chemical freeze-out temperature $T_{\rm ch}$. Whereas at kinetic freeze-out defined by the temperature $T_{\rm kin}$, elastic interactions among the particles cease fixing the particles momenta.

We use the transverse momentum ($p_{\rm T}$) spectra of identified particles in HICs to study the above-mentioned bulk properties. We can also extract the freeze-out parameters, T_{ch} and T_{kin} by fitting the data to thermal equilibrium model and hydrodynamics-motivated blast-wave model respectively.

4.1.1 Event Selection

Please find the event selection described in section 3.1 of the chapter on Centrality determination (previous chapter).

4.1.2 Track Selection

For optimal particle identification, we select the good tracks through the application of cuts. To study the identified particle spectra, the distance of closest approach (DCA) of the tracks from the event vertex are taken to be less than 3 cm. A rapidity cut of $|y| < 0.1$ is used. The cut on the number of fit points (nFitPts) should be 25 to avoid split tracks (one track counted as two). The tracks travelling through the TPC volume can have maximum 45 possible hits. The fraction of points used in the fit is required to be greater than 0.52 of the maximum fit points (nFitPoss) to prevent over counting of split tracks. In order to ensure tracks have good $\langle dE/dx \rangle$, a cut is applied on the number of hits used to calculate $\langle dE/dx \rangle$ of the track i.e., nHitsdEdx > 15.

To summarize,

- $-0.1 < y < 0.1$
- DCA < 3 cm
- nHitsFit > 25
- $\frac{\text{nHitsFit}}{\text{nHitsPoss}} > 0.52$
- nHitsdEdx > 15

4.2 Particle Identification

For particle identification, we use the energy loss (dE/dx) information from TPC. The below shows dE/dx as function of the ratio of momentum and charge for Au+^{3}He collisions at $\sqrt{s_{NN}} = 200$GeV.

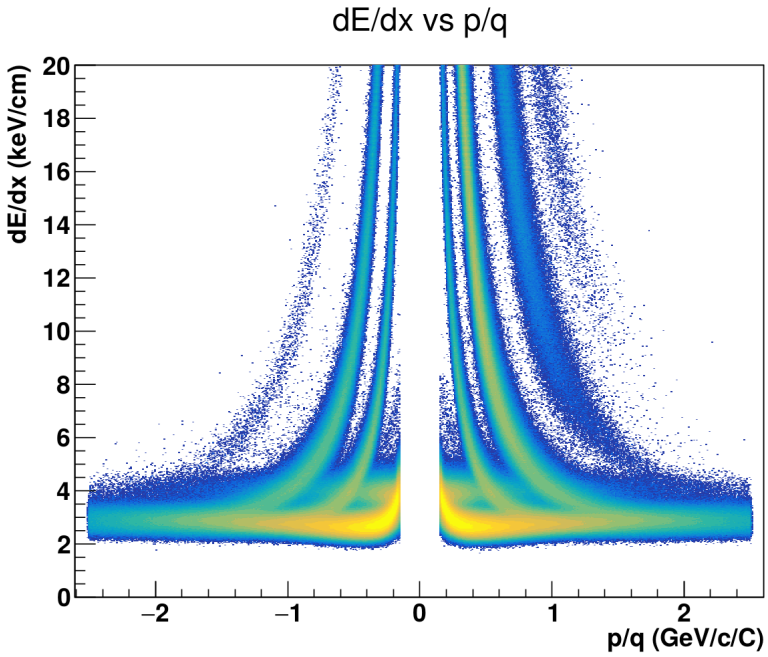

Figure 4.1: The dE/dx distribution of charged particles with $|y| < 0.1$ as a function of (momentum/charge) in Au-^{3}He collisions at $\sqrt{s_{NN}} = 200$GeV. The left part shows negatively charged particles and the right part shoes positively charged particles.

However, as the $\langle dE/dx \rangle$ distribution for a particle is not Gaussian, for ease of particle identification (via multi-Gaussian fitting), we define a new variable for a particular particle i as,

$$Z_i = \ln \left[\frac{(\frac{dE}{dx})_{\text{experiment}}}{(\frac{dE}{dx})_{\text{theory}}} \right] \tag{4.1}$$

$(\frac{dE}{dx})_{theory}$ was calculated using the Bischel function (an approximation of Bethe bloch energy loss formula) as,

$$\left(\frac{dE}{dx} \right)_{\text{theory}} = q^2 \exp \left(B \left(\log_{10} \left(\frac{p|q|}{M_{\text{part}}} \right) \right) \right) \tag{4.2}$$

Where, q = charge, p = momentum, $M_{\text{part}} = M_\pi$ or M_K or M_{proton}. B is the Bischel function. [16]

For a given particle, Z_i distributions are made in different p_T bins within rapidity $|y| < 0.1$. To extract the raw yeild of a particular particle in a given p_T bin, we

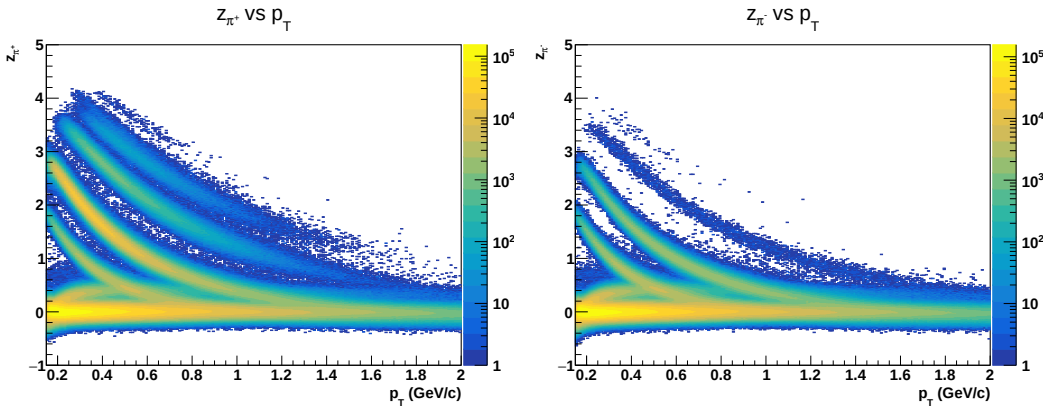

Figure 4.2: The Z variable distributions for π^+ (left) and π^- (right) with $|y| < 0.1$ in Au-^{3}He collisions at $\sqrt{s_{NN}} = 200$GeV.

perform a multi-Gaussian fit to the Z_i distribution. The multi-Gaussian is given by:

$$f(z) = \frac{b.w.}{\sqrt{2\pi}}\Big(\sum_{j=1}^{4}\frac{N_j}{\sigma_j}\exp\Big[\frac{z-M_j}{z\sigma_j^2}\Big]\Big) \tag{4.3}$$

Here, $b.w.$ is the bin width and N_i are the required yeilds.

After the yeild is obtained in each p_T bins, we plot the yeild vs. p_T to get the transverse momentum spectra.

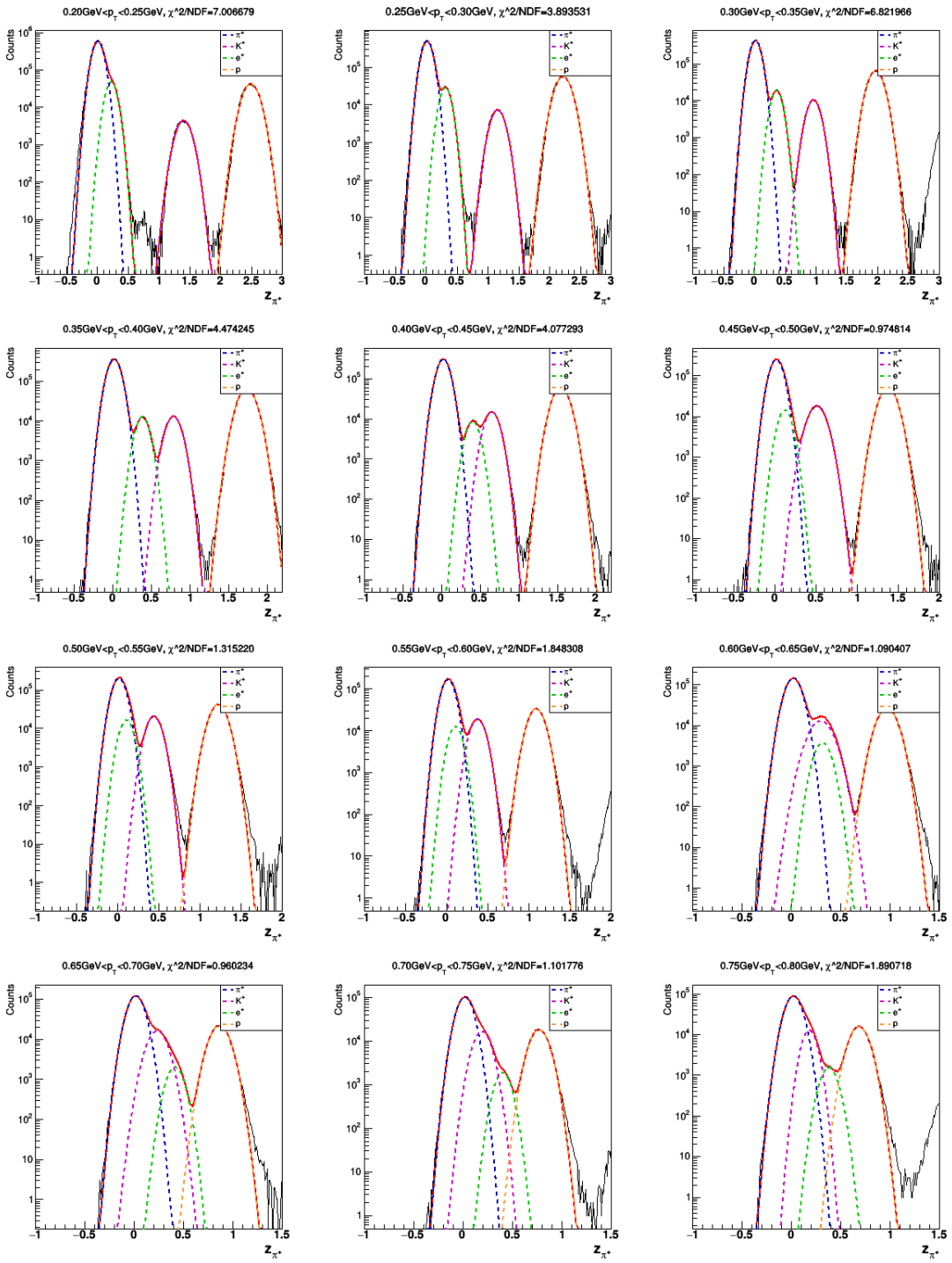

Figure 4.3: The Z_π distribution of π^+ for different p_T bins in Au+^{3}He collisions at $\sqrt{s_{NN}}$ = 200 GeV. The curves are Gaussian fits representing contributions from pions (dotted- blue), electrons (dotted-green), kaons (dotted-magenta), and protons (dotted-orange).

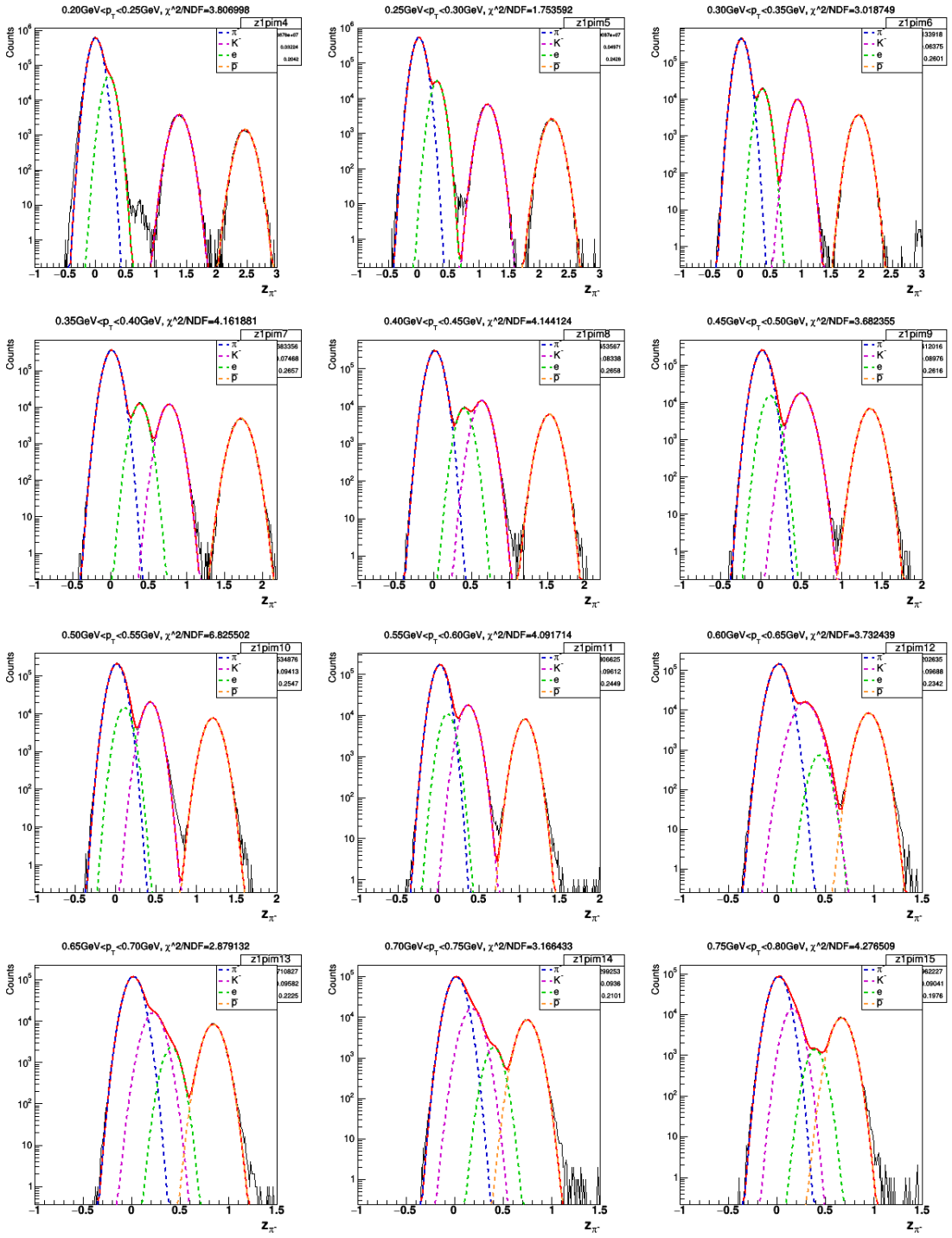

Figure 4.4: The Z_π distribution of π^- for different p_T bins in Au+^{3}He collisions at $\sqrt{s_{NN}}$ = 200 GeV. The curves are Gaussian fits representing contributions from pions (dotted- blue), electrons (dotted-green), kaons (dotted-magenta), and protons (dotted-orange).

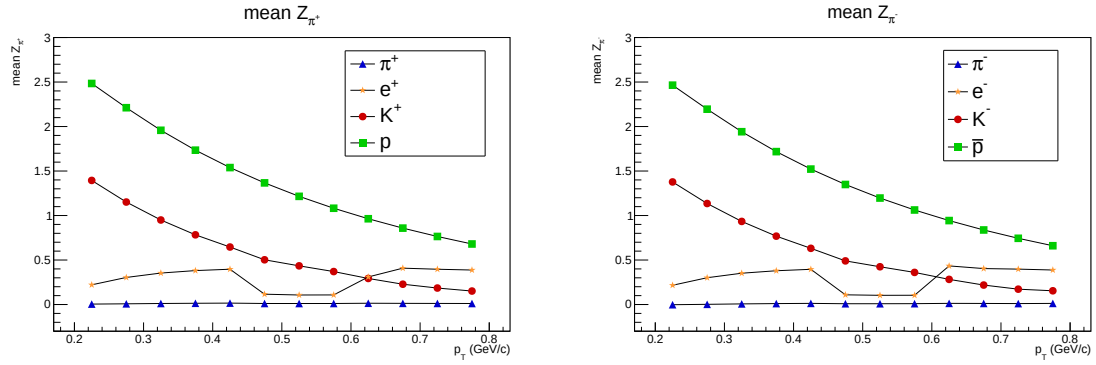

Figure 4.5: Mean positions of diferent particles in z_π distribution as a function of p_T. The left figure shows the means of z_π distribution of π^+ and the right figure shows the means of z_π distribution of π^-. The plots are made for particles with $|y| < 0.1$ in Au-^{3}He collisions at $\sqrt{s_{NN}} = 200$GeV.

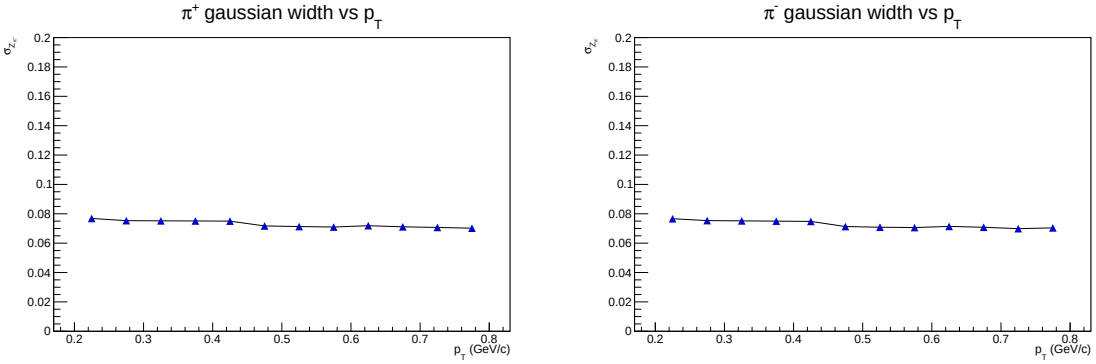

Figure 4.6: Width of the pion gaussian as a function of p_T. The left figure is for z_π distribution of π^+ and the right figure is for z_π distribution of π^-.

We see that the means of the gaussians in a p_T bin plotted with p_T traces the peaks of the 2-D Z_π vs p_T distribution in Fig. 4.2, which is expected. The width of the $\pi^\pm$ gaussians dont vary much with p_T and stays flat.

We normalize the yeilds in every p_T bin with the total number of events and plot it with p_T, this plot is called the minimun bias p_T spectra. In figure 4.7, we see a clear dependence of normalized yeilds with p_T for both π^+ and π^-. The yeilds decrease monotonically with increasing p_T.

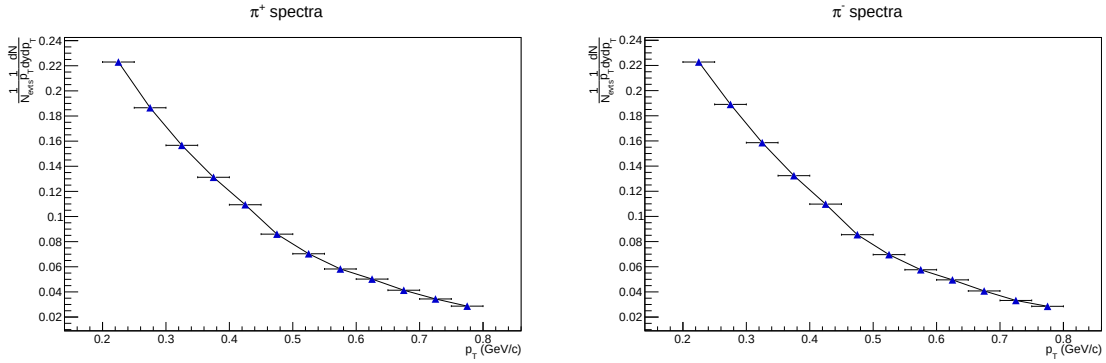

Figure 4.7: Normalized minimum bias π^+ (left) and π^-(right) yeilds as functions of p_T . The plots are made for particles with $|y| < 0.1$ in Au-^{3}He collisions at $\sqrt{s_{NN}} = 200$GeV.

Similar procedures of plotting p_{T} spectra was done in different centralities and for all particles (π, K, p). The below graph is made for π^+. We see that the shape of π^+ spectra remains same in different centralities.

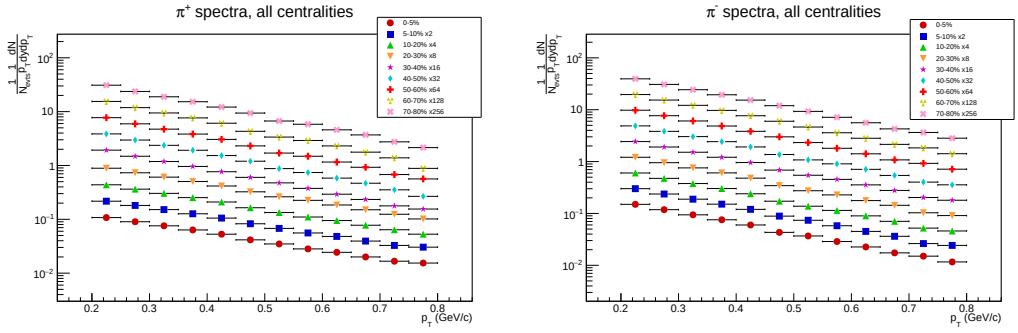

Figure 4.8: p_T spectra of π^+ in different centralities. The graphs were scaled by some factors relative to the 70-80% plot to increase visibility.

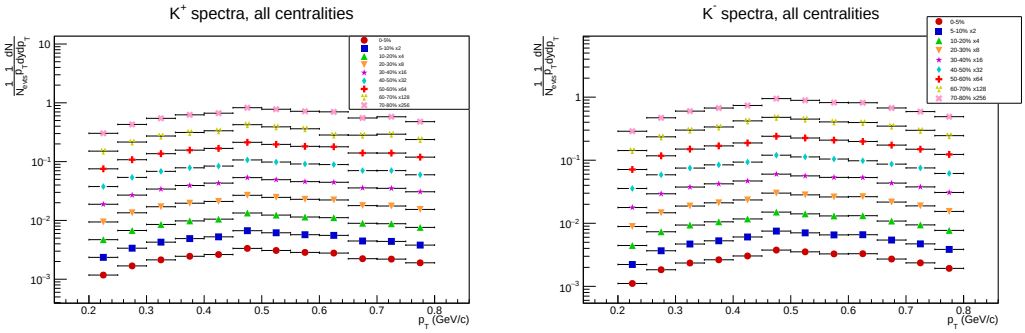

Figure 4.9: p_T spectra of π^+ in different centralities. The graphs were scaled by some factors relative to the 70-80% plot to increase visibility. The plots are made for particles with $|y| < 0.1$ in Au-^{3}He collisions at $\sqrt{s_{NN}} = 200$GeV.

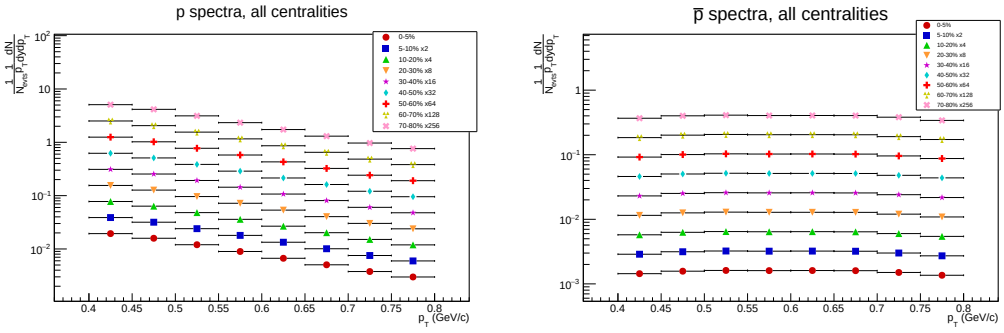

Figure 4.10: p_T spectra of π^+ in different centralities. The graphs were scaled by some factors relative to the 70-80% plot to increase visibility. The plots are made for particles with $|y| < 0.1$ in Au-^{3}He collisions at $\sqrt{s_{NN}} = 200$GeV.

4.2.1 Particle identification and spectra from TOF

As we can see in the Figs. 4.2, 4.3 and 4.4, after 0.7-0.8 GeV, the particle tracks of pion, kaon, electron and protons start merging together. Hence, particle identification from TPC in higher p_T bins becomes more difficult and less reliable. So, we use the time of flight information from the TOF detector for pushing the particle identification to higher p_T.

From TOF, we find the spectra using m^2 distribution in different p_T bins. m^2 is

calculated as,

$$m^2 = p^2 \left(\frac{c^2 T^2}{l^2} - 1 \right) \tag{4.4}$$

Here, T = time of flight, l = pathlength, p = momentum, c = speed of light. However, finding the yeilds in each p_T bins is not as straight forward as in the case of TPC, as the m^2 distribution for a given particle is not gaussian. So, Instead of doing a multi-gaussian fit, we fit out m^2 distribution with a sum of predicted m^2 distribution for each particle under consideration[34][35].

First we calculate an expected time of flight, $T_{expected}$ for a particular hadron using the PDG value of the mass of the hadron.

$$T^{had}_{exp} = \frac{l}{c} \Big(\frac{m^2_{had}}{p^2} + 1 \Big)^{1/2} \tag{4.5}$$

Where, $had = \pi$, K or p

Then we calculate $\Delta t^{had} = T - T^{had}_{exp}$ and fill it into a histogram for each p_T bin. The histograms for each hadron (π, K, p) are filled subject to a cut, $n\sigma_{had} < 2.0$ (PID selection).

In another event loop, we calculate $T^{had}_{predicted} = T^{had}_{exp} + \Delta t^{had}_{random}$ where, Δt^{had}_{random} is randomly sampled from the Δt^{had} distribution for each p_T bin. Using T^{had}_{pred}, we calculate $m^2_{pred,had}$ as,

$$m^2_{pred,had} = p^2 \left(\frac{c^2 (T^{had}_{pred})^2}{l^2} - 1 \right) \tag{4.6}$$

Thus, after obtaining m^2_π, m^2_K and m^2_p in a particular p_T bin, we add these histograms and fit it to the total m^2 distribution in that p_T bin, with the scaling factors of the histograms as free parameters.

The yeilds in each p_T bin is obtained by integrating the scaled histograms.

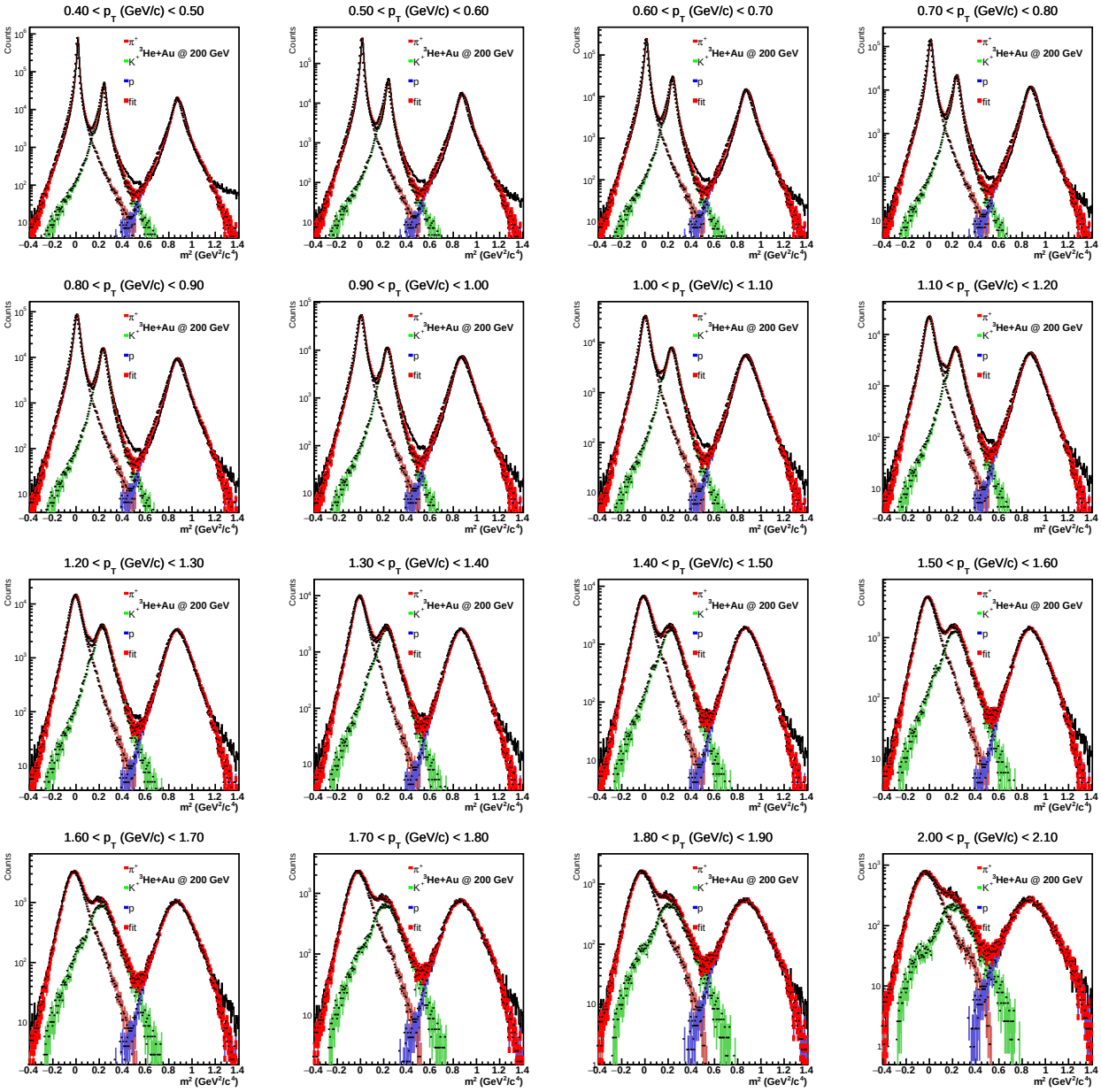

Figure 4.11: The predicted m^2 fitting for positively charged identified hadrons is shown here for all p_T bins at 0-5% centrality in Au-^{3}He collisions at $\sqrt{s_{NN}} = 200$GeV. The plots are made for particles with $|y| < 0.1$ in Au-^{3}He collisions at $\sqrt{s_{NN}} = 200$GeV.

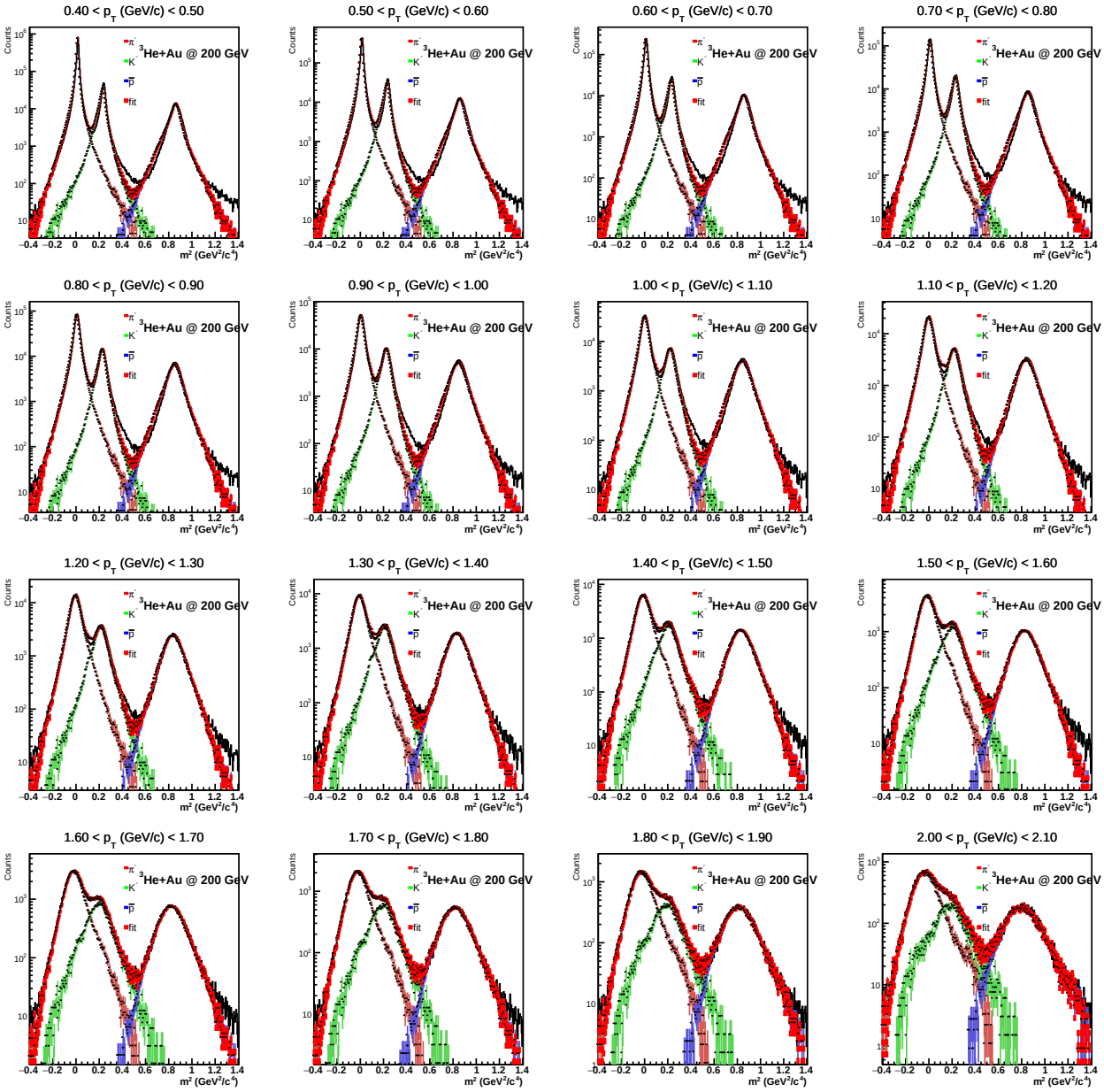

Figure 4.12: The predicted m^2 fitting for negatively charged identified hadrons is shown here for all p_T bins at 0-5% centrality in Au-^{3}He collisions at $\sqrt{s_{NN}} = 200$GeV. The plots are made for particles with $|y| < 0.1$ in Au-^{3}He collisions at $\sqrt{s_{NN}} = 200$GeV.

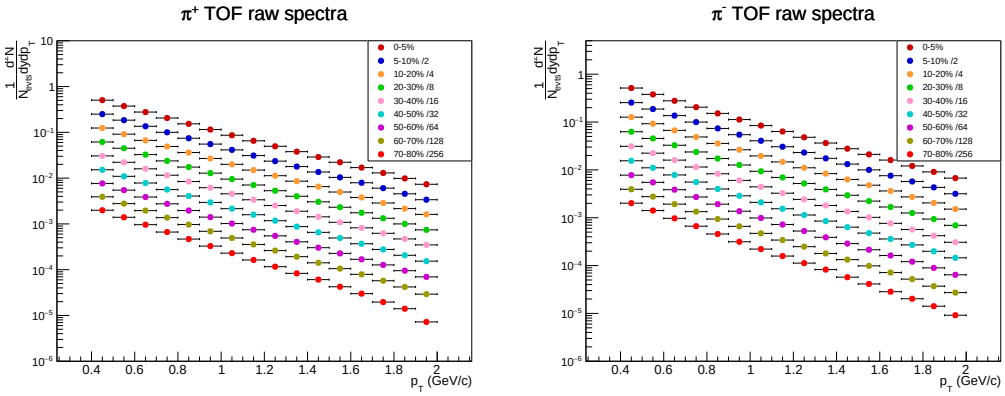

Figure 4.13: (Left) The π^+ spectra from TOF in different centralities. (Right) The π^- spectra in different centralities. The spectras in other centralities are scaled by powers of 2 w.r.t $0-5\%$ for visibility. The plots are made for particles with $|y| < 0.1$ in Au-^{3}He collisions at $\sqrt{s_{NN}} = 200$GeV.

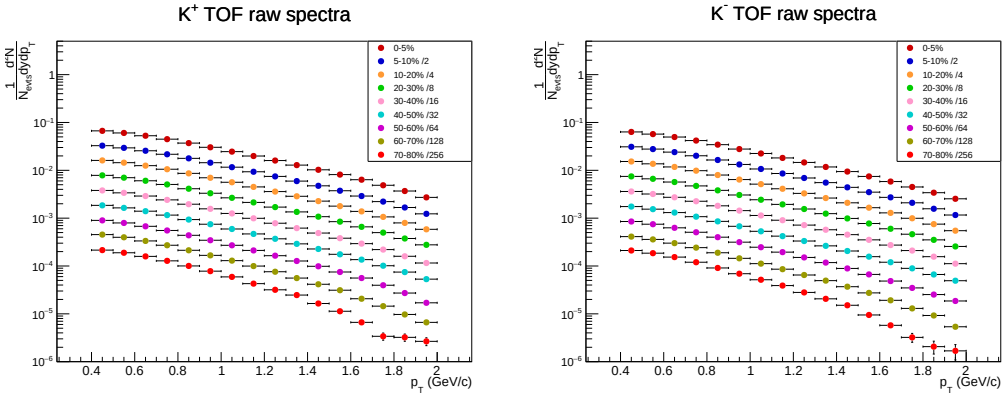

Figure 4.14: (Left) The K^+ spectra from TOF in different centralities. (Right) The K^- spectra in different centralities. The spectras in other centralities are scaled by powers of 2 w.r.t $0-5\%$ for visibility. The plots are made for particles with $|y| < 0.1$ in Au-^{3}He collisions at $\sqrt{s_{NN}} = 200$GeV.

From the plots, we see that, the shape of pion raw spectra remains mostly identical in all centralities. Whereas, On the other hand, the slope of kaon and proton spectra shows a gradual flattening as one goes from peripheral to central collisions. This is an indication of stronger radial flow effects for heavier particles with increasing centrality.

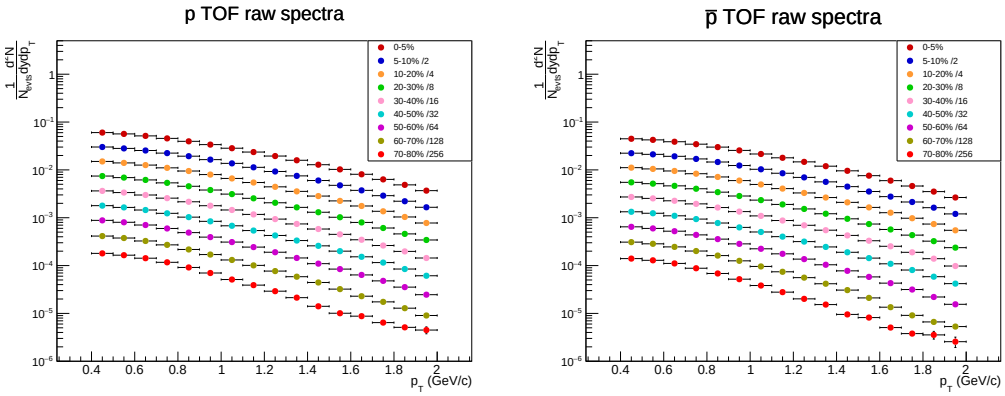

Figure 4.15: (Left) The p spectra from TOF in different centralities. (Right) The $\bar{p}$ spectra in different centralities. The spectras in other centralities are scaled by powers of 2 w.r.t $0-5\%$ for visibility. The plots are made for particles with $|y| < 0.1$ in Au-^{3}He collisions at $\sqrt{s_{NN}} = 200$GeV.

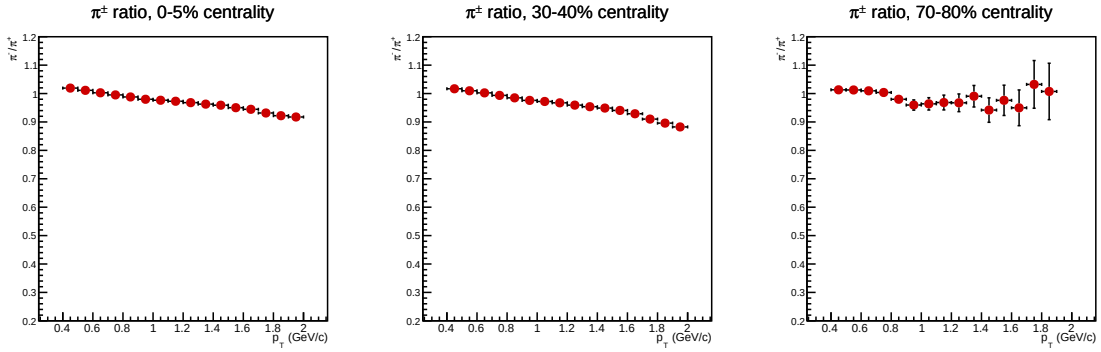

Figure 4.16: π^-/π^+ in different p_T bins, in $0-5\%$ (Left), $30-40\%$ (Middle) and $50-60\%$ (Right) centralities. The plots are made for particles with $|y| < 0.1$ in Au-^{3}He collisions at $\sqrt{s_{NN}} = 200$GeV.

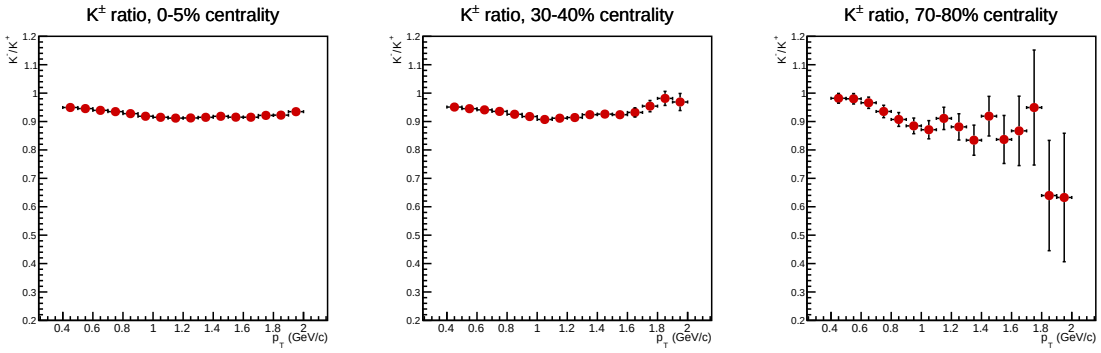

Figure 4.17: K^-/K^+ in different p_T bins, in $0-5\%$ (Left), $30-40\%$ (Middle) and $50-60\%$ (Right) centralities. The plots are made for particles with $|y| < 0.1$ in Au-^{3}He collisions at $\sqrt{s_{NN}} = 200$GeV.

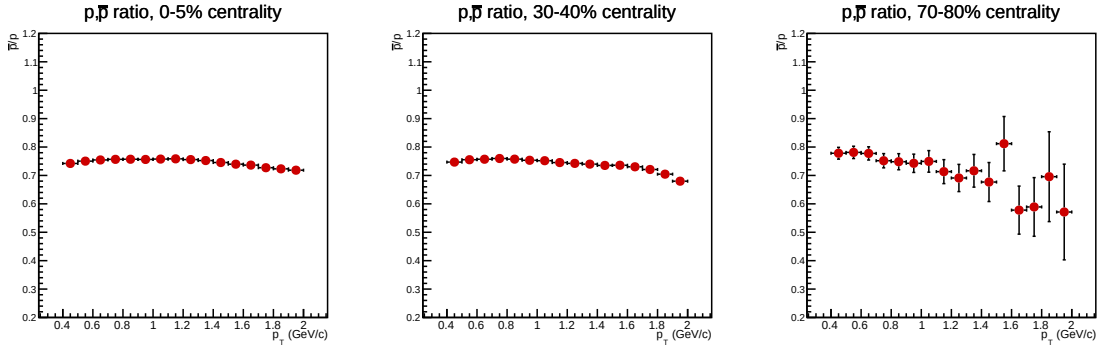

Figure 4.18: $\bar{p}/p$ in different p_T bins, in $0-5\%$ (Left), $30-40\%$ (Middle) and $50-60\%$ (Right) centralities. The plots are made for particles with $|y| < 0.1$ in Au-^{3}He collisions at $\sqrt{s_{NN}} = 200$GeV.

4.3 Correction factors

The raw spectra extracted in the earlier sections are not the true spectra, as they are associated with detector inefficiency as well as contamination from various sources. Corrections need to be performed on the raw p_T spectra to extract any meaningful physics from it. The first step in performing these corrections is a process embedding technique, which is a monte carlo simulation [28][29][30].

4.3.1 Monte-Carlo Embedding Technique

Simulated events are generated from a flat p_T and η distribution using Heavy Ion Jet Interaction Generator (HIJING)[31] to ensure equal statistics in each p_T bin. These generated tracks are called embedded tracks with initial momentum p_T^{MC}. It is then mixed with the real events at 5% level and is allowed to pass through the GSTAR[32] (the software package to run STAR detector simulation using GEANT[33]) and TRS (the TPC response simulator). The data is reconstructed as that of the real data taking into consideration all the detector effects. Then a association mapping is performed between the reconstructed tracks and the input MC tracks. For each MC track in GEANT, a search for reconstructed track is performed within a window of $\pm$0.6cm in x, y and z [29]. If the track is found, then the reconstructed track is marked as matched track. If more than 10 hits of the MC track match with a single reconstructed track in the embedded event, then the track is called a reconstructed track with a momentum assigned p_T^{REC}. After this a quality assurance of the embedding sample is done to make sure that the MC simulation sample reproduces the characteristics of real data. For this, we compare distributions such as DCA, nFitpoints, nHits dEdx and ϕ between real data.

Using information from the embedding data, we correct the raw p_T spectra bin by bin. *Unfortunately, the embedding simulation could not be completed in time for the submission of this report, so, as of now, no correction to the data could be done.*

4.4 Summary and Outlook

- We have implemented the methods for finding raw p_T spectra of $\pi^{\pm}$, $K^{\pm}$, $p(\bar{p})$ in all centralities from TPC and TOF.

- Efficiency, acceptance, and other corrections will be performed once the embed-

ding data is ready.

- The corrected spectra will be fitted to various appropriate distribution function to extract $\langle p_T \rangle$ and dN/dy dependence.
- The corrected spectra will be fitted to Blast-wave function to extract freezeout parameters.

Chapter 5

A Multi-Phase Transport (AMPT) model

A Multi-Phase Transport(AMPT) Model is a Monte-Carlo transport model for heavy ion collision at high energies or relativistic velocities [46]. Being a transport model, it treats the non-equilibrium dynamics explicitly and includes both partonic interactions that occurs initially and the subsequent hadronic interactions. The model has been coded using Fortan 77. The current version used in the project is v1.26. The AMPT model has two different variations representing different physics, the default AMPT model and the AMPT model with string melting.

The AMPT model consists of the following components:

- **Heavy Ion Jet Interaction Generator (HIJING):** The initial conditions of the collision are obtained using the HIJING model. It is a two component model consisting of soft strings and hard minijets. The initial consitions consist of the spatial and momentum distributions of minijet partons and soft string excitations for a collision.

- **Zhangs parton cascade (ZPC):** Partonic interactions is modelled using the ZPC model which models the scatterings among partons. It includes only two-body scatterings with cross sections obtained from the pQCD with screening masses. This is an event driven simulation as the observables are calculated at the point when the next interaction takes place.

- **Lund string fragmentation model:** In the AMPT default model, the con-

version from the partonic to the hadronic matter is through the recombination of the par- tons with their parent strings after the parton interactions have terminated. The resulting strings are then converted to hadrons using the Lund string fragmentation model.

- **Quark coalescence model:** In the AMPT model with string melting, once the partons stop interacting, they combine into hadrons using the Quark coalescence model. The hadrons then interact using the extended ART model.

- **Extended A Relativistic Transport (ART) model:** The ART model is used to simulate the subsequent hadronic interactions, and extended to include additional reaction channels that are significant at high energies. This is time driven simulation as the coordinates of the particles are calculated at fixed intervals of time.

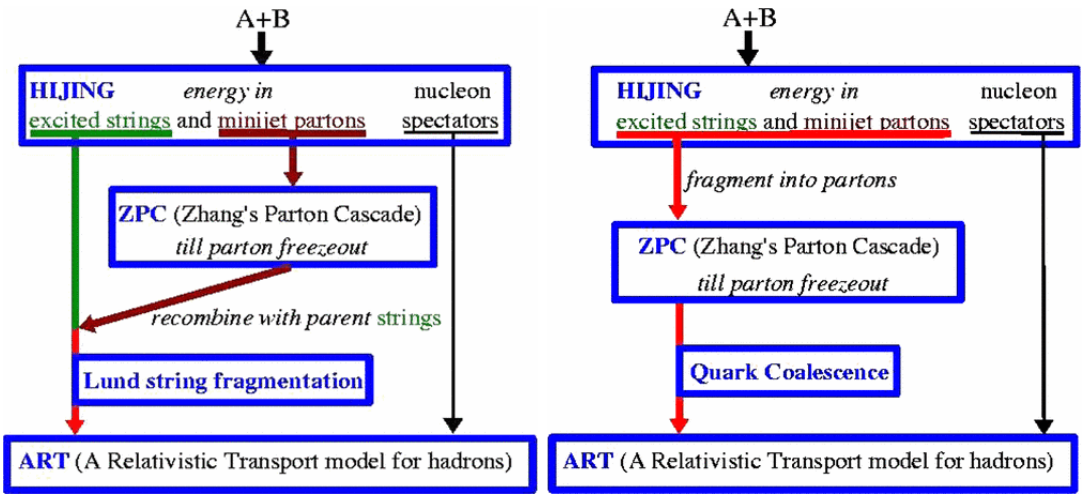

Figure 5.1: AMPT model schematic, in default format (left) and with string melting turned on (right) [46].

Once the hadronic interactions are terminated, the final output is obtained after a threshold time t_{cut} at which point all interactions are terminated. The observables are

considered to be stable at that point and it is assumed that no more of the hadronic interactions would lead to significant change to the observables.

5.1 Spectra analysis from AMPT data

For the rest of the analysis in this chapter, we have used AMPT with String melting turned on and partonic cross section σ_p 3mb. A total of 3.5 million 200GeV Au-^{3}He events were generated. Centrality determination was done by applying cuts on the RefMult distribution (number of charged particles with $|\eta| < 0.5$ in an event). Higher RefMults correspond to higher centralities. All the analyses below have been done at mid rapidity (track cut of $|y| < 0.1$) has been applied.

5.2 Transverse momentum spectra

p_T spectra is obtained from AMPT data directly by filling separate p_T histograms for π, K, p in different centralities. The $\pi^{\pm}$ spectra have similar shape in all centralities.

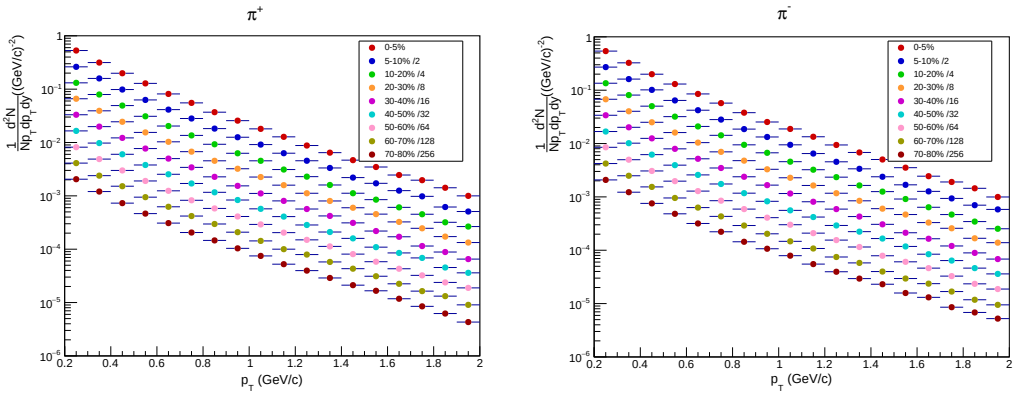

Figure 5.2: (Left) Spectra for π^+ in different centralities. (Right) Spectra for π^- in different centralities.

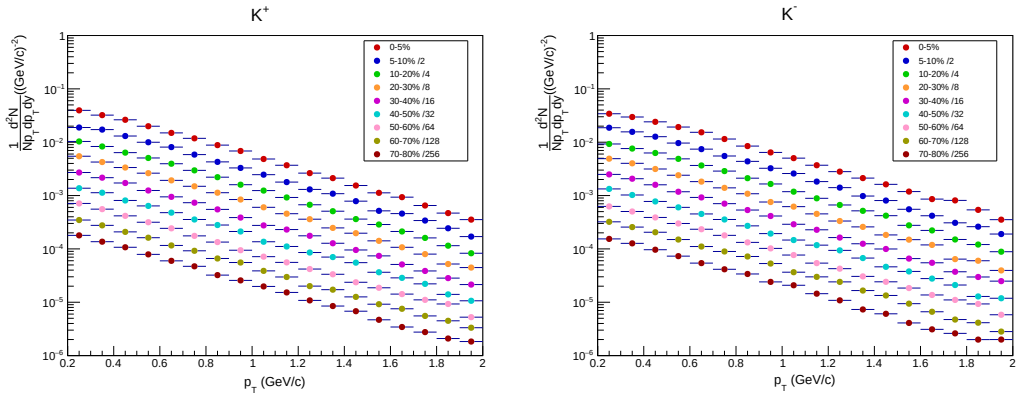

Figure 5.3: (Left) Spectra for K^+ in different centralities. (Right) Spectra for K^- in different centralities.

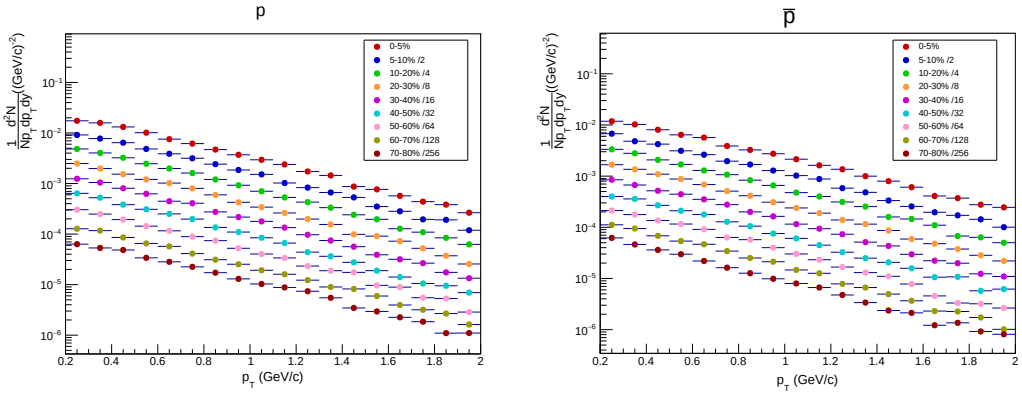

Figure 5.4: (Left) Spectra for p in different centralities. (Right) Spectra for $\bar{p}$ in different centralities.

The obtained p_T spectra are fitted with appropriate distribution functions. The fit functions are Bose-Einstein for pions, m_T - exponential for kaons and double exponential for (anti) protons. These fit functions are so chosen that, it best describes the spectral shape of the particle.

for $\pi^{\pm}$

Functional form of the fit function (Bose-Einstien): $c_{\mathrm{BE}} \left[\exp\left(\frac{m_{\mathrm{T}}}{T_{\mathrm{BE}}}\right) - 1\right]^{-1}$

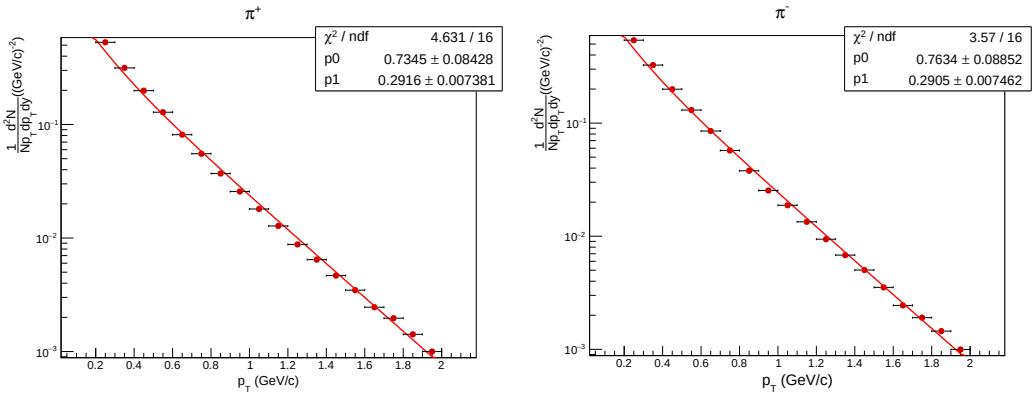

Figure 5.5: (Left) Fitting for π^+. (Right) Fitting for π^-. Here, $p0 = c_{\mathrm{BE}}$ and $p1 = T_{\mathrm{BE}}$.

for $K^{\pm}$

Functional form of the fit function (m_T exponential): $c_{m_{\mathrm{T}}} \exp\left[\frac{-(m_{\mathrm{T}}-m)}{T_{m_{\mathrm{T}}}}\right]$

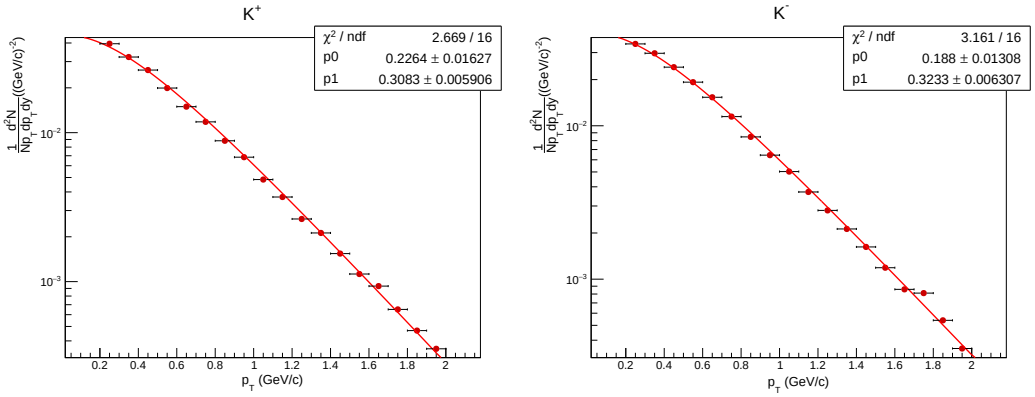

Figure 5.6: (Left) Fitting for K^+. (Right) Fitting for K^-. Here, $p0 = c_{\mathrm{m_T}}$ and $p1 = T_{\mathrm{m_T}}$.

for $p(\bar{p})$

Functional form of the fit function (Double exponential): $c_1 \exp\left(\frac{-p_{\mathrm{T}}^2}{T_1^2}\right) + c_2 \exp\left(\frac{-p_{\mathrm{T}}^2}{T_2^2}\right)$

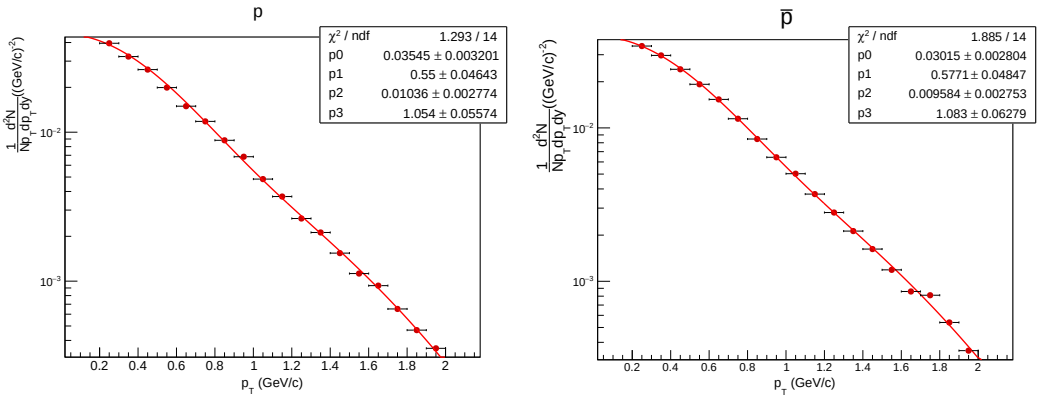

Figure 5.7: (Left) Fitting for p. (Right) Fitting for $\bar{p}$. Here, $p0 = c_1$, $p1 = T_1$, $p2 = c_2$ and $p3 = T_2$.

5.3 Average transverse momentum

Average transverse momenta quantitatively characterizes the slope of the measured p_T spectra of the particles and can be studied in terms of collision energy and centrality. i.e., the transverse dynamics of the particles is reflected in terms of $\langle p_T \rangle$. It is calculated as,

$$\langle p_T \rangle = \frac{\int p_T 2\pi p_T f\left(p_T\right) dp_T}{\int 2\pi p_T f\left(p_T\right) dp_T} \tag{5.1}$$

where, $f(p_T)$ is the function used to fit the p_T spectra of the particles. The integration is performed in the p_T range of 0-10 GeV/c. We see that the $\langle p_T \rangle$ stays flat and shows low dependence on centrality.

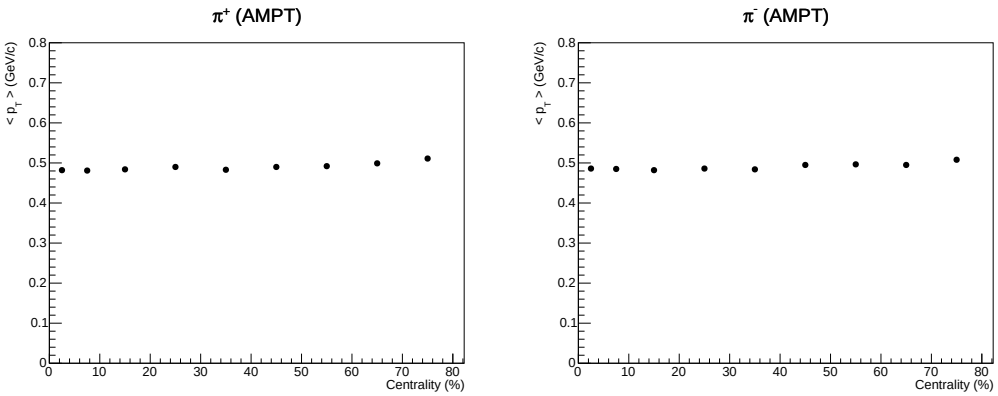

Figure 5.8: $\langle p_T \rangle$ vs Centrality plot for π^+ (Left) and π^- (Right).

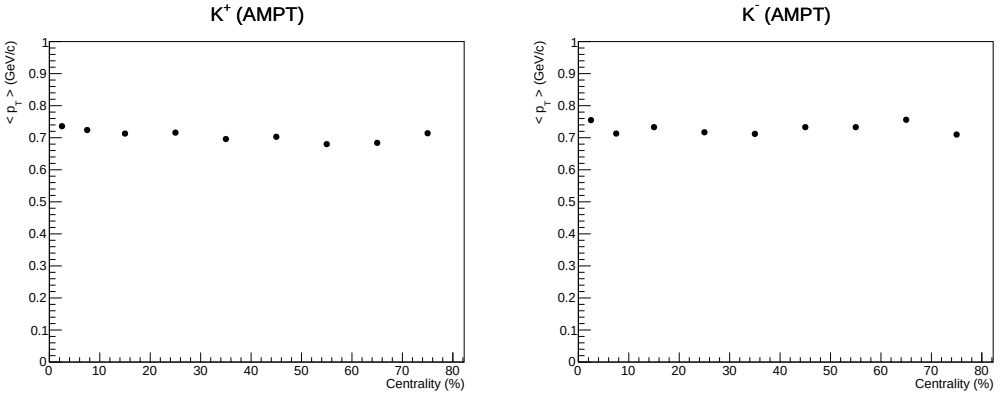

Figure 5.9: $\langle p_T \rangle$ vs Centrality plot for K^+ (Left) and $K-$ (Right).

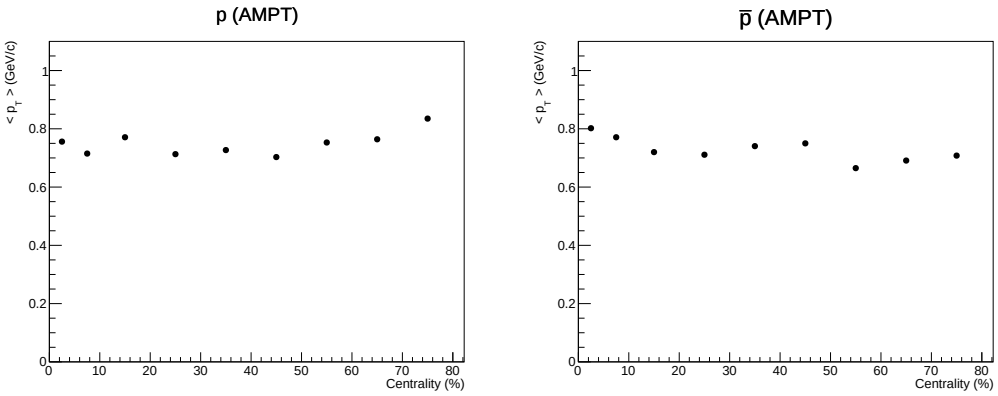

Figure 5.10: $\langle p_T \rangle$ vs Centrality plot for p (Left) and $\bar{p}$ (Right).

5.4 Particle yeilds

The total particle abundance is a reflective of the total entropy produced in the collision. In a particular collision centrality at midrapidity ($|y| < 0.1$), it is defined by dN/dy or particle yield. This is obtained by integrating the p_T spectra of the particles over p_T. It is calculated as,

$$\frac{dN}{dy} = \int f\left(p_T\right) 2\pi p_T dp_T \tag{5.2}$$

and

Where, $f(p_T)$ are the fitted distributions. We see that, in all cases, except for the most peripheral centrality bin, the dN/dy decreases with decreasing centrality.

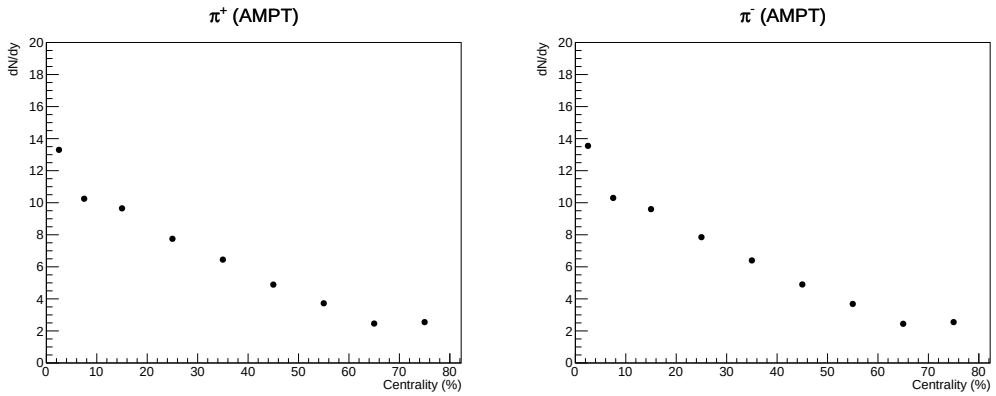

Figure 5.11: dN/dy vs Centrality plot for π^+ (Left) and π^- (Right).

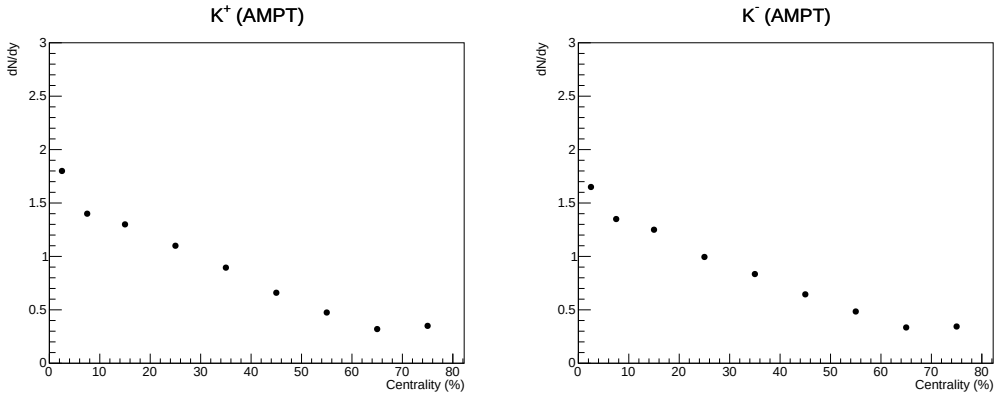

Figure 5.12: dN/dy vs Centrality plot for K^+ (Left) and K^- (Right).

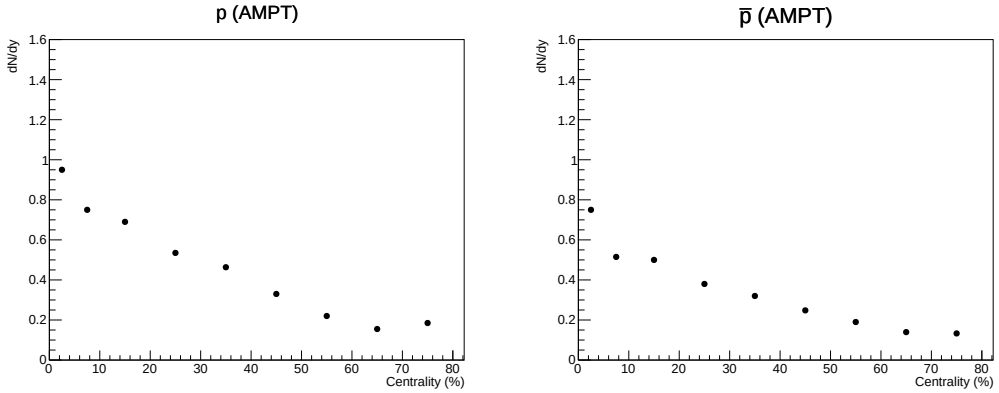

Figure 5.13: dN/dy vs Centrality plot for p (Left) and $\bar{p}$ (Right).

5.5 Kinetic freezeout

Next, we use the p_T spectra ro extract the kinetic freeze-out properties. These properties characterize the details of the systems at kinetic freeze-out or when the elastic collisions of the particles stops. During this stage, the key parameters used to characterize the system are the temperature and radial expansion velocity. We obtain the kinetic freeze-out parameters by fitting the p_T spectra to a hydrodynamics-motivated blast-wave model[36][37]. The model assumes local thermalization of the particles at the kinetic freeze-out temperature and that the they are moving with a common

transverse flow velocity field. Assuming a radially boosted thermal source with a transverse radial flow velocity β_T and a kinetic freeze-out temperature T_{kin}, the p_T spectra of the particles is parametrized as follows:

$$\frac{1}{p_T}\frac{dN}{dp_T} \propto \int_0^R r dr m_T I_0\left(\frac{p_T \sinh\rho}{T_{\rm kin}}\right) K_1\left(\frac{m_T \cosh\rho}{T_{\rm kin}}\right) \tag{5.3}$$

Where, I_0 and K_1 are the modified Bessel functions of the first and second kind respectively, $m_T = \sqrt{p_T^2 + m^2}$ is the transverse mass, r is the transverse radial distance, R is the radius of the fireball.

ρ is the velocity profile given by,

$$\rho = \tanh^{-1}\beta_{\rm T} = \tanh^{-1}\left(\left(\frac{r}{R}\right)^n \beta_s\right) \tag{5.4}$$

With β_T being the transverse expansion velocity, and β_s is the maximum transverse expansion velocity (at the surface of the fireball).

From these equations, we can also derive the average transverse expansion velocity $\langle\beta_T\rangle = \frac{n}{n+2}\beta_n$. We keep the freeze-out temperature T_{kin}, the average transverse velocity $\langle\beta_T\rangle$, and the exponent of the velocity profile n as free parameters in our fits. We simultaneously fit the$\pi^{\pm}$, $K^{\pm}$ and $p(\bar{p})$particle spectra with the blast-wave model.

The fit was done using TMinuit package in ROOT to acomplish χ^2 minimization. Due to the low multiplicity of the Au-^{3}He events, we have taken wider centrality bins to compensate for that. In the figure below, we see that the fits for $p(\bar{p})$ degrades rapidly at higher p_T.

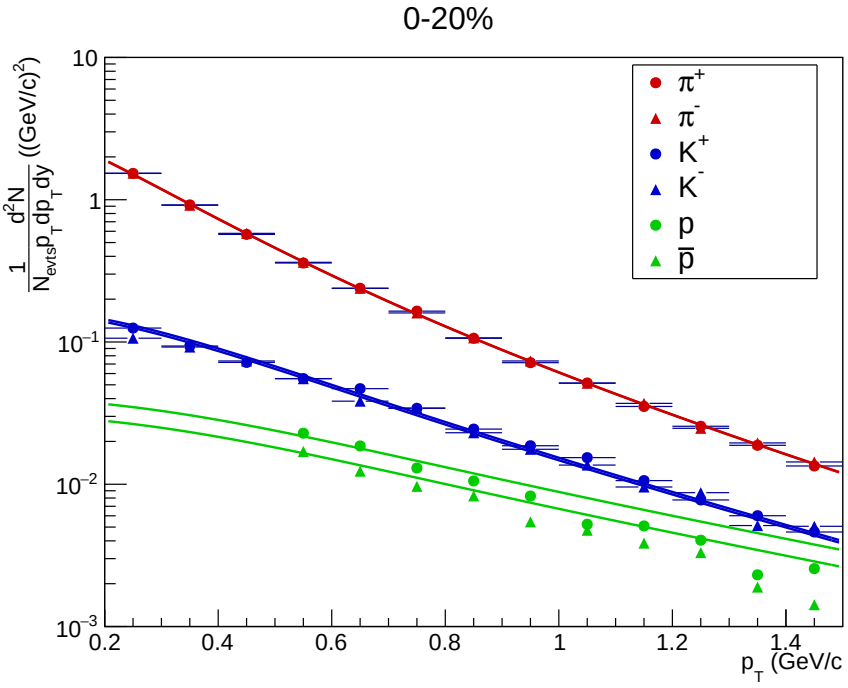

Figure 5.14: Blast-wave fits for $\pi^{\pm}$, $K^{\pm}$ and $p(\bar{p})$ in 0-20% centrality bin.

Centrality (%)	$T_{kin}(MeV)$	$\langle\beta_T\rangle$	n	χ^2/NDF
0-20	118 ± 4	0.463 ± 0.015	1.784 ± 0.129	69.14
20-40	120 ± 5	0.444 ± 0.019	2.014 ± 0.18	58.67
40-60	123 ± 7	0.42 ± 0.026	2.326 ± 0.233	37.87
60-100	112 ± 7	0.472 ± 0.025	1.98 ± 0.205	25.33

Table 5.1: Parameters T_{kin}, $\langle\beta_T\rangle$, n in different centrality bins.

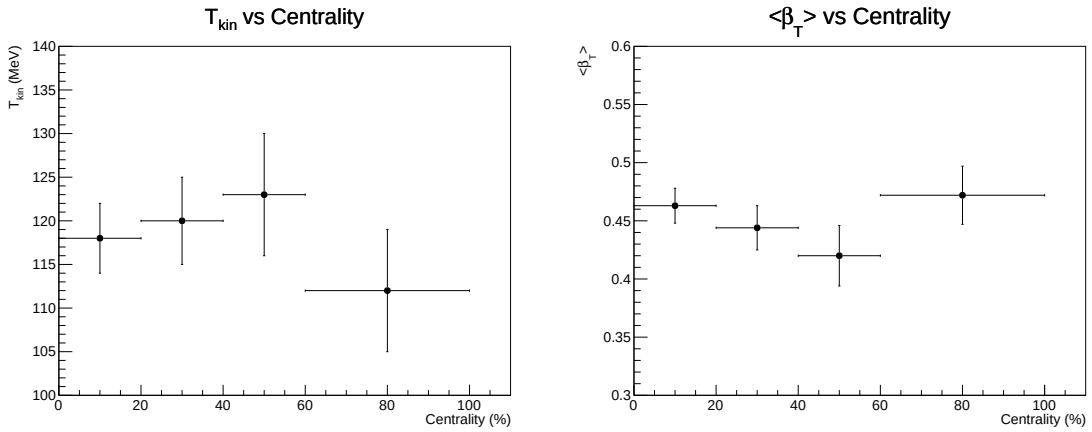

Figure 5.15: (Left) Kinetic freezeout temperature (T_{kin}) vs. Centrality, (Right) Average transverse velocity ($\langle\beta_T\rangle$) vs. Centrality.

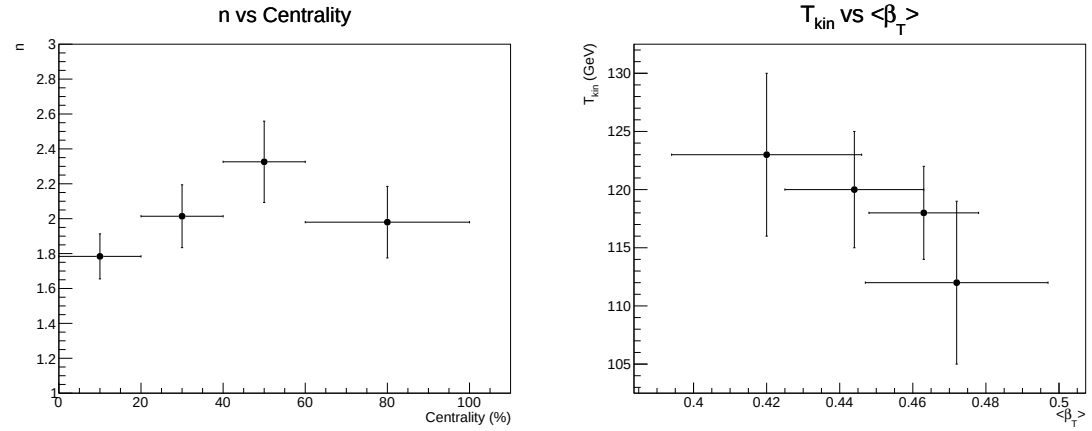

Figure 5.16: (Left) Exponent of velocity profile (n) vs. Centrality, (Right) T_{kin} vs. $\langle\beta_T\rangle$.

5.6 Summary and Outlook

- The transverse momentum spectra of $\pi^{\pm}$, $K^{\pm}$ and $p(\bar{p})$ at midrapidity ($|y| < 0.1$) are measured for nine centralities.
- Observables like average transverse momentum ($\langle p_T\rangle$), particle yields (dN/dy) and kinetic freeze-out properties are extracted
- We need to repeat everything in a higher statistics to improve the fits.

- One could try to see tha variation of the freeze-out properties by varying σ_{pp}.
- Next step would be to do all of the above excercises on efficiency corrected real data.

Appendix A

Modified ^{3}He distribution

A.1 The Hamiltonian

We assume the simplest picture of a nucleus, a nonrelativistic system of interacting nucleons (neutrons and protons), whose Hamiltonian is given by,

$$\sum_i \frac{\mathbf{p}_i^2}{2m} + \sum_{i<j} v_{ij} + \sum_{i<j<k} V_{ijk} + \cdots \tag{A.1}$$

The nucleons can interact via two-, three-, or many-body interactions. The first term is the kinetic energy term, and the subsequent terms represent the 2 and 3 body interactions. [19]

A.1.1 Two - nucleons (NN) interactions

The NN interactions are given by Argonne v_{18}(AV18) interactions.[20] The AV18 potential is written as a sum of electromagnetic term, one-pion-exchange term and a short-range phenomenological part, [18]

$$v_{ij} = v_{ij}^{\gamma} + v_{ij}^{\pi} + v_{ij}^{R} \tag{A.2}$$

The electromagnetic terms include one- and two- photon exchange Coulomb interaction, vacuum polarization, Darwin-Foldy, and magnetic moment terms, with appropriate proton and neutron form factors:

$$\begin{aligned} v^{\gamma}(pp) &= V_{C1}(pp) + V_{C2} + V_{vp} + V_{DF} + V_{MM}(pp) \\ v^{\gamma}(np) &= V_{C1}(np) + V_{MM}(np) \\ v^{\gamma}(nn) &= V_{MM}(nn) \end{aligned} \tag{A.3}$$

The long-range component of the NN interaction is due to one-pion exchange (OPE). Ignoring the isospin-breaking terms, it can be written at long distances as,

$$\begin{array}{l} v_{ij}^{\pi} = \frac{f_{\pi NN}^2}{4\pi} \frac{m_\pi}{3} \left[Y_\pi \left(r_{ij} \right) \boldsymbol{\sigma}_i \cdot \boldsymbol{\sigma}_j + T_\pi \left(r_{ij} \right) S_{ij} \right] \boldsymbol{\tau}_i \cdot \boldsymbol{\tau}_j \\ Y_\pi \left(r_{ij} \right) = \frac{e^{-\mu r_{ij}}}{\mu r_{ij}} \\ T_\pi \left(r_{ij} \right) = \left[1 + \frac{3}{\mu r_{ij}} + \frac{3}{\left(\mu r_{ij} \right)^2} \right] \frac{e^{-\mu r_{ij}}}{\mu r_{ij}} \end{array} \tag{A.4}$$

Where, the mass m_π is the mass of the exchanged pion, $\boldsymbol{\sigma}_i$ and $\boldsymbol{\tau}_i$ are spin and isospin operators and $S_{ij} \equiv 3\boldsymbol{\sigma}_i \cdot \hat{\mathbf{r}}_{ij} \boldsymbol{\sigma}_j \cdot \hat{\mathbf{r}}_{ij} - \boldsymbol{\sigma}_i \cdot \boldsymbol{\sigma}_j$

The one-pion-exchange and the remaining phenomenological part of the potential is written as a sum of 18 operators,

$$v_{ij}^{\pi} + v_{ij}^{R} = \sum_{p=1,18} v_p \left(r_{ij} \right) O_{ij}^{p} \tag{A.5}$$

The first 14 are charge independent and the last 4 break the charge independence.

$$O_{ij}^{p=1,14} = \left[1, \left(\sigma_i \cdot \sigma_j \right), S_{ij}, \left(\mathbf{L} \cdot \mathbf{S} \right), \mathbf{L}^2, \mathbf{L}^2 \left(\sigma_i \cdot \sigma_j \right), \left(\mathbf{L} \cdot \mathbf{S} \right)^2 \right] \otimes \left[1, \left(\tau_i \cdot \tau_j \right) \right] \tag{A.6}$$

$$O_{ij}^{p=15,18} = \left[1, \left(\sigma_i \cdot \sigma_j \right), S_{ij} \right] \otimes T_{ij}, \left(\tau_{zi} + \tau_{zj} \right) \tag{A.7}$$

The coefficients are obtained by fitting the potential to nucleon-nucleon scattering data

A.1.2 Three nucleon (NNN) interactions

The Urbana series of three-nucleon potentials can be written as sum of a two-pion-exchange term and a short-range phenomenological term, [18]

$$V_{ijk} = V_{ijk}^{2\pi} + V_{ijk}^{R} \tag{A.8}$$

The two pion exchange potential and the phenomenological potential are given by:

$$V_{ijk}^{2\pi} = A_{2\pi} [\{X_{ij}, X_{ik}\}\{\tau_i \cdot \tau_j, \tau_i \cdot \tau_k\} + \frac{1}{4} [X_{ij}, X_{ik}][\tau_i \cdot \tau_j, \tau_i \cdot \tau_k]] \tag{A.9}$$

Where, $X_{ij} = Y_\pi(r_{ij})\,\boldsymbol{\sigma}_i \cdot \boldsymbol{\sigma}_j + T_\pi(r_{ij})\,S_{ij}$

$$V_{ijk}^R = U_0 \sum_{\text{cyc}} T_\pi^2(r_{ij})\,T_\pi^2(r_{ik}) \tag{A.10}$$

The parameters for model IX are $A_{2\pi} = 0.0293$ MeV and $U_0 = 0.0048$ MeV [19]. They have been determined by fitting the density of nuclear matter and the binding energy of ^3H in conjunction with the AV18 interaction.

A.2 The trial wave-function

A.2.1 Variational Monte Carlo

Variational Monte Carlo (VMC) explicitly writes a trial wave function, with 20-30 variational parameters. Optimization of the parameters is done by minimizing the expectation value of energy. Spatial integrals are evaluated using the Metropolis algorithm.

The trial wave functions used in VMC calculations typically have a simple form [19]:

$$|\Psi_T\rangle = \left[\mathcal{S}\prod_{i<j<k} F_{ijk}\right]\left[\mathcal{S}\prod_{i<j} F_{ij}\right]|\Psi_J\rangle \tag{A.11}$$

Here , the Jastrow state $|\Psi_J\rangle$ carries the quantum number information. The Jastrow wave function $|\Psi_J\rangle$ is given by,

$$|\Psi_J\rangle = \mathcal{A}\left[\prod_{i<j\in \text{s}} f_{\text{ss}}^c(r_{ij}) \prod_{i\in \text{s}, j\in \text{p}} f_{\text{sp}}^c(r_{ij}) \prod_{i\in \text{p}, j\in \text{p}} f_{\text{pp}}^c(r_{ij})\,|\Phi(JMTT_z)\rangle\right] \tag{A.12}$$

f^c's are the central-pair correlation functions dependent the pair distance only. At long distances, the behavior may be different for nucleons in different shells, and hence label the f^c's by the single-particle orbits of the two nucleons.

The two-body spin-isospin correlation operators F_{ij} in the equation for $|\Psi_T\rangle$ carry

the short- and intermediate-range physics. They are parametrized as

$$F_{ij} = \left[1 + \sum_{m=2,8} u_m\left(\mathbf{r}_{ij};\mathbf{R}\right) O_{ij}^m\right] \tag{A.13}$$

and contain operators O_{ij}^m that are a subset of those employed in the interaction:

$$O_{ij}^m = [1, \boldsymbol{\sigma}_i \cdot \boldsymbol{\sigma}_j, S_{ij}, (\mathbf{L}\cdot\mathbf{S})_{ij}] \otimes [1, \boldsymbol{\tau}_i \cdot \boldsymbol{\tau}_j] \tag{A.14}$$

The dependence upon the pair distance r_{ij} is obtained as a solution of Schrdinger like equations in the various two-body channels. Schematically, they are written as,

$$-(1/m)\nabla^2[f(r)\phi(\mathbf{r})]_{JST} + [v_{ij} + \lambda(r)]\,[f(r)\phi(\mathbf{r})]_{JST} = 0 \tag{A.15}$$

We solve the equation for the various channels of J, S, T and the correlations are rewritten in operator form. The functions $\phi(r)$ contain the appropriate spherical harmonics for the given J, S, T. For the spin-triplet channels the combination $[f(r)\phi(\mathbf{r})]_{JST}$ satisfies two coupled equations with $L = J - 1$ and $L = J + 1$. The variational parameters are included in the functional form of $\lambda(r)$. For s-shell nuclei, the form is adjusted so that

$$[f_{\rm ss}^c(r)]^{A-1} \to \exp(-\gamma r)/r \tag{A.16}$$

where γ is related to the separation energy of the last nucleon.

The structure of the three-nucleon correlations F_{ijk} is derived frim NNN interaction V_{ijk}

$$F_{ijk} = 1 - \beta V_{ijk} \tag{A.17}$$

where β is again a variational parameter.

Typically, one uses the Metropolis method to obtain points distributed pro- portional to a probability density $W(\mathbf{R})$, often choosing $W(\mathbf{R}) = |\langle\Psi_T(\mathbf{R})|\Psi_T(\mathbf{R})\rangle|$,

where the angle brackets indicate sums over the internal degrees of freedom, the spins and isospins. Hence expectation value can be estimated as,

$$\langle O\rangle = \frac{\int d\mathbf{R}\,\langle\Psi_T(\mathbf{R})|O|\Psi_T(\mathbf{R})\rangle}{\int d\mathbf{R}\,\langle\Psi_T(\mathbf{R})|\Psi_T(\mathbf{R})\rangle} \approx \frac{\sum_i \langle\Psi_T\left(\mathbf{R}_i\right)|O|\Psi_T\left(\mathbf{R}_i\right)\rangle / W\left(\mathbf{R}_i\right)}{\sum_i \langle\Psi_T\left(\mathbf{R}_i\right)\Psi_T\left(\mathbf{R}_i\right)\rangle / W\left(\mathbf{R}_i\right)} \tag{A.18}$$

Replacing O with R, we can calculate an upper bound to the exact ground-state energy,

$$E = \frac{\langle\Psi_T|H|\Psi_T\rangle}{\langle\Psi_T|\Psi_T\rangle} \geqslant E_0 \tag{A.19}$$

A.3 Green's function Monte Carlo

The basis of this technique is using Green's function as an propagator:

$$|\Psi_0\rangle = \lim_{\tau\to\infty} \exp\left[-\left(H - E_0\right)\tau\right]|\Psi_T\rangle \tag{A.20}$$

For a short period of imaginary time,

$$|\Psi(\tau+\Delta\tau)\rangle = \exp\left[-\left(H - E_0\right)\Delta\tau\right]|\Psi(\tau)\rangle \tag{A.21}$$

matrix elements of the short-time propagator:

$$\begin{aligned}
&\langle\mathbf{R}',\chi'|\exp(-H\Delta\tau)|\mathbf{R},\chi\rangle \\
&\quad = G\left(\mathbf{R}',\mathbf{R};\Delta\tau\right) \approx \left[\prod_{i=1,A} G_{0,i}\left(|\mathbf{r}_i - \mathbf{r}'_i|\right)\right] \\
&\quad \times \sum_{\chi_1,\chi_2} \left\langle\chi'\left|\left[1 - \frac{\Delta\tau}{2}\sum_{i\leq j<k} V_{ijk}\left(\mathbf{R}'\right)\right]\right|\chi_1\right\rangle \\
&\quad \times \left\langle\chi_1\left|S\prod_{i<j}\left[\frac{g_{ij}\left(\mathbf{r}'_{ij},\mathbf{r}_{ij}\right)}{\left(g_{0ij}\left(\mathbf{r}'_{ij},\mathbf{r}_{ij}\right)\right.}\right]\right|\mathcal{X}_2\right\rangle\langle\chi_2| \\
&\quad \times \left[1 - \frac{\Delta\tau}{2}\sum_{i<j<k} V_{ijk}(\mathbf{R})\right]|\chi\rangle
\end{aligned} \tag{A.22}$$

Here, g_{0ij} and G_0 are the free one and two body propagators.

A very general scheme of GFMC is given here:

- The trial wavefunction (Ψ_T) is obtained by using variation of parameters, and a set of coordinates is sampled from the distribution $|\Psi_T^2|$.

- For each configuration, the subsequent configurations $\mathbf{R_i}$, at $\tau = i\Delta\tau$, are obtained sequentially from R_{i-1}, by iterating with the importance-sampled Greens function G_I ,

$$I\left(\mathbf{R}_i\right)\Psi\left(\mathbf{R}_i\right) = \int G_I\left(\mathbf{R}_i, \mathbf{R}_{i-1}\right) I\left(\mathbf{R}_{i-1}\right)\Psi\left(\mathbf{R}_{i-1}\right) d\mathbf{R}_{i-1} \tag{A.23}$$

  Where,

$$G_I\left(\mathbf{R}_i, \mathbf{R}_{i-1}\right) = \left[I\left(\mathbf{R}_i\right) G\left(\mathbf{R}_i, \mathbf{R}_{i-1}\right) \frac{1}{I\left(\mathbf{R}_{i-1}\right)}\right] \tag{A.24}$$

  and,

$$I(\mathbf{R}) = |\Psi_T(\mathbf{R})| \tag{A.25}$$

- Each configuration is iterated until it converges to ground state.

Appendix B

Comparision of Modified and Unmodified ^{3}He nuclear profile

We need to compare the ^{3}He nuclear profiles from the GFMC calculations (Modified) and the default nuclear profile in AMPT (Unmodified). To that end, we generated two implementations of AMPT with String melting turned on and $\sigma_{pp} = 3$mb for the two ^{3}He configurations. The two ^{3}He implementations have also been compared with Au-Au collisions from AMPT and STAR data.

To compare the two nuclear profiles, we need to use bulk observables which are dependent on initial conditions, i.e., anisotropic flow, eccentricity, pearson correlation, symmetric cumulants, etc.

B.1 Pearson correlation coefficient

Pearson's correlation coefficient is the covariance of the two variables divided by the product of their standard deviations. The form of the definition involves a "product moment", that is, the mean (the first moment about the origin) of the product of the mean-adjusted random variables[38].

$$\rho_{X,Y} = \frac{\mathrm{E}\left[\left(X - \mu_X\right)\left(Y - \mu_Y\right)\right]}{\sigma_X \sigma_Y} \tag{B.1}$$

Here, σ_i is the standard deviation of variable i, μ_i is the mean of the variable i,the operator E is the expectation.

Expanding the numerator and denominator of the above eqaution, we get the expression of ρ in terms of the uncentered moments.

$$\rho_{X,Y} = \frac{\mathrm{E}[XY] - \mathrm{E}[X]\mathrm{E}[Y]}{\sqrt{\mathrm{E}\left[X^2\right] - [\mathrm{E}[X]]^2}\sqrt{\mathrm{E}\left[Y^2\right] - [\mathrm{E}[Y]]^2}} \tag{B.2}$$

We have plotted the pearson correlation between the two protons in ^{3}He vs. impact parameter(b) for the two ^{3}He configurations.

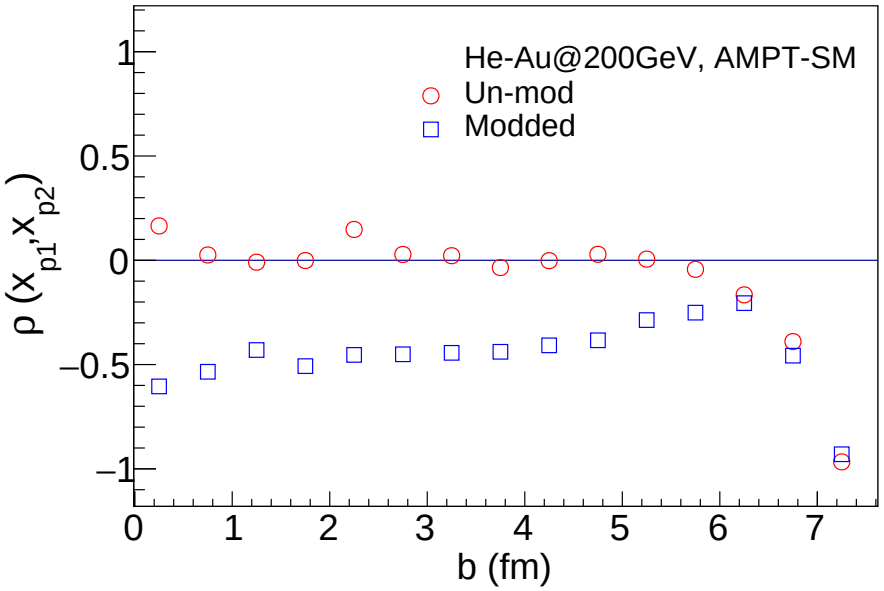

Figure B.1: $\rho(x_{p1}, x_{p2})$ vs. b plot. We can see that $\rho(x_{p1}, x_{p2})$ is nearly zero for unmodified profile, whereas the modified profile shows some negative correlation. (This plot was made by Dr. Rihan Haque)

B.2 Eccentricity

Mathematically, the participant eccentricity is given as [39],

$$\varepsilon_2 = \frac{\sqrt{\left(\sigma_y^2 - \sigma_x^2\right)^2 + 4\left(\sigma_{xy}\right)^2}}{\sigma_y^2 + \sigma_x^2} \tag{B.3}$$

Where, for an event, σ_X^2, σ_Y^2 are the variances and σ_{XY} is the covariance of the participating nucleon distribution in the transverse direction.If we shift the coordinates so that $\langle X \rangle$ and $\langle Y \rangle$ are equal to zero. we can show that,

$$\varepsilon_2 = \frac{\sqrt{\langle r^2 \cos\left(2\phi_{\mathrm{part}}\right)\rangle^2 + \langle r^2 \sin\left(2\phi_{\mathrm{part}}\right)\rangle^2}}{\langle r^2 \rangle} \tag{B.4}$$

Where, $(r\ ,\phi_{part})$ are polar coordinate positions of participant nucleons.

Similarly, we can find triangularity ϵ_3 as,

$$\varepsilon_3 \equiv \frac{\sqrt{\langle r^2 \cos(3\phi_{\rm pat})\rangle^2 + \langle r^2 \sin(3\phi_{\rm part})\rangle^2}}{\langle r^2 \rangle} \tag{B.5}$$

We have plotted the ϵ_2 and ϵ_3 as a function of number of charged particles in an event(N_{ch}) and number of participants (N_{part}) for both the ^{3}He configurations.

From the figures 7.2 to 7.5, we can see that the eccentricities and triangularities calculated from modified and unmodified ^{3}He nuclear profiles are different. From the ratio plots of $\epsilon_{2,3}$, we conclude that the unmodified case shows higher $\epsilon_{2,3}$ than the modified case in almost all $N_{\rm ch}$ and $N_{\rm part}$ bins.

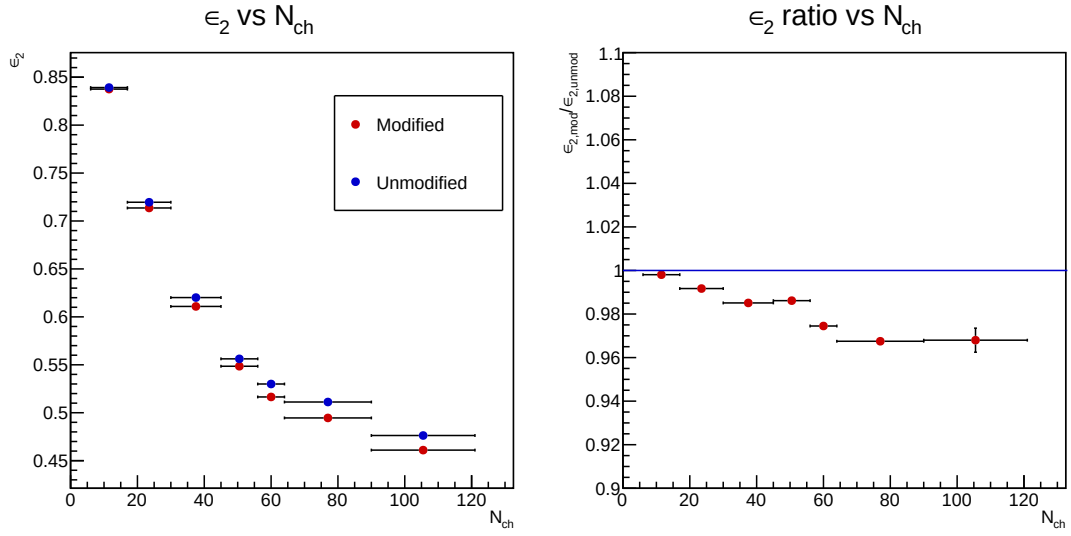

Figure B.2: (Left) Plot of ϵ_2 vs. N_{ch} for Modified(red) and Unmodified(blue) cases. (Right) Ratio of ϵ_2 in modified and unmodified cases. We see that ϵ_2 in unmodified case is a little higher than the modified case.

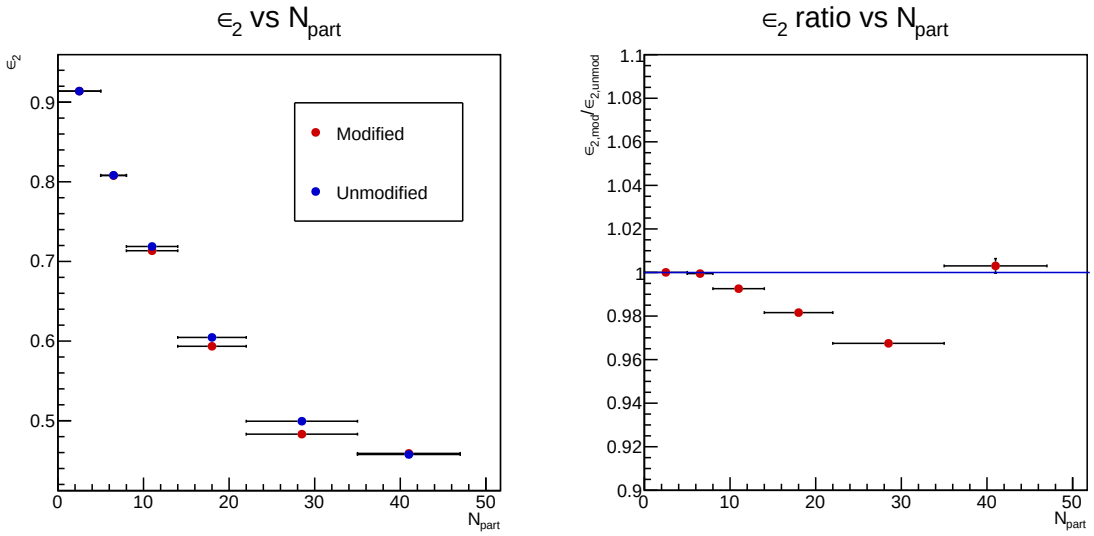

Figure B.3: (Left) Plot of ϵ_2 vs. N_{part} for Modified(red) and Unmodified(blue) cases. (Right) Ratio of ϵ_2 in modified and unmodified cases.

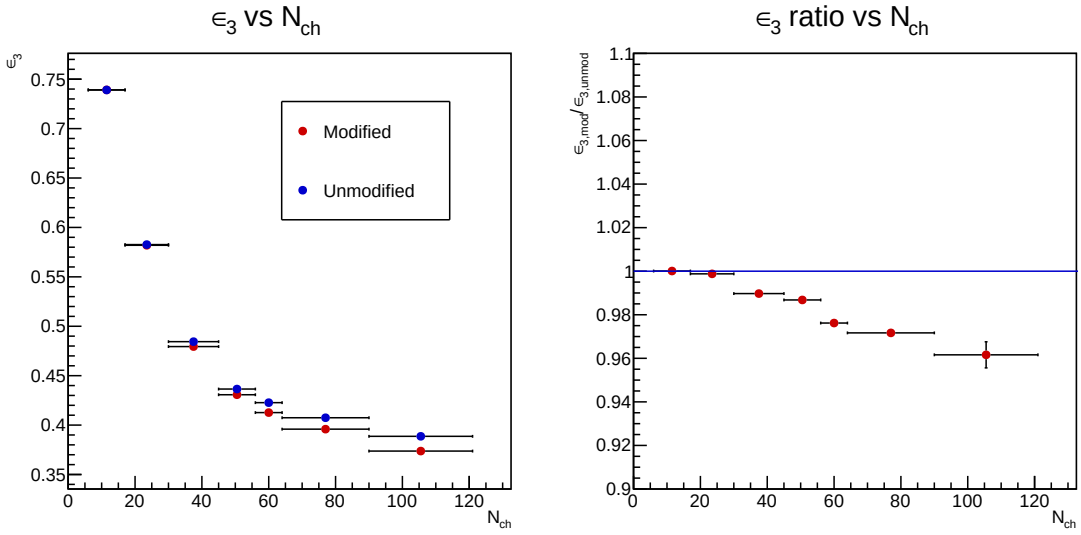

Figure B.4: (Left) Plot of ϵ_3 vs. N_{ch} for Modified(red) and Unmodified(blue) cases. (Right) Ratio of ϵ_3 in modified and unmodified cases. We see that ϵ_3 in unmodified case is a little higher than the modified case.

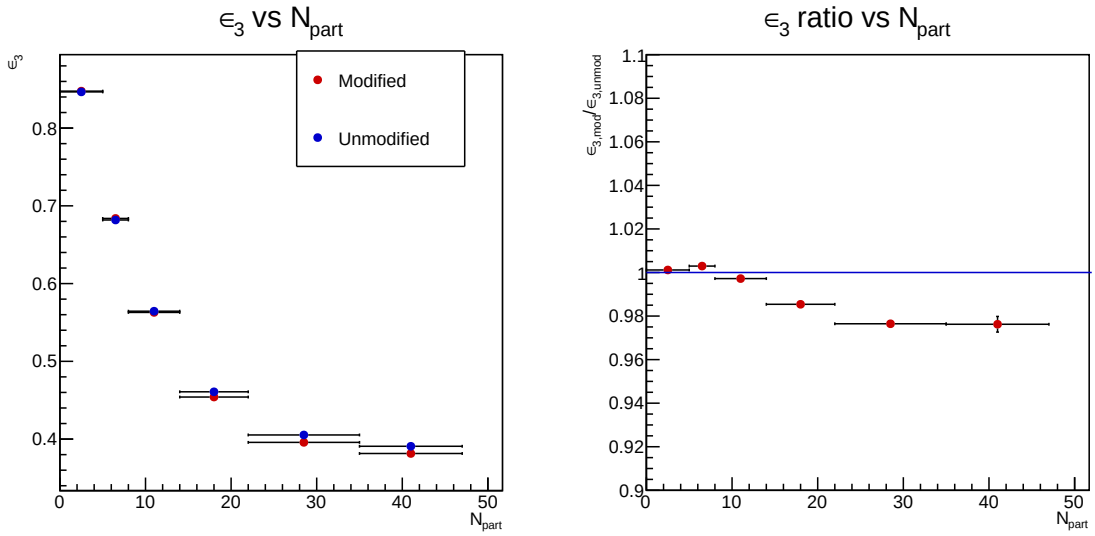

Figure B.5: (Left) Plot of ϵ_3 vs. N_{part} for Modified(red) and Unmodified(blue) cases. (Right) Ratio of ϵ_3 in modified and unmodified cases.

For both ϵ_2 and ϵ_3 we see that the N_{ch} dependence shows more change with change in nuclear profile than the N_{part} dependence.

B.3 Anisotropic flow

The anisotropic flow parameters v_n are good tools for studying initial conditions in QGP . They describe the momentum anisotropy of particle emission from non-central heavy-ion collisions. They are obtained from the harmonic coefficients of the Fourier expansion of the azimuthal distribution w.r.t event plane angle (Ψ_r) and can be written as [40]

$$E\frac{d^3N}{d^3p} = \frac{1}{2\pi}\frac{d^2N}{p_t dp_t dy}\left(1 + \sum_{n=1}^{\infty} 2v_n \cos\left(n\left(\phi - \Psi_p\right)\right)\right) \tag{B.6}$$

and the nth fourier coefficient is given by, $\langle\cos(n(\phi - \Psi_p))\rangle$. $\langle\rangle$ denotes average over all particles in all events.

Event plane is the plane containing the beam and the impact parameter. We

can estimate n^{th} order event plane from the polar coordinates of the participating nucleons as, [39]

$$\psi_n = \frac{\operatorname{atan} 2\left(\left\langle r^2 \sin\left(n\phi_{\text{pat}}\right)\right\rangle, \left\langle r^2 \cos\left(n\phi_{\text{part}}\right)\right\rangle\right) + \pi}{n} \tag{B.7}$$

So, anisotropic flow, v_n is defined as,

$$v_n = \langle \cos\left(n\left(\phi - \psi_n\right)\right)\rangle \tag{B.8}$$

B.3.1 Flow from 2-particle correlators

For a particular event,

$$\langle 2\rangle \equiv \left\langle e^{in(\phi_1-\phi_2)}\right\rangle \equiv \frac{1}{P_{M,2}} \Sigma'_{i,j} e^{in(\phi_i-\phi_3)} = \frac{|Q_n|^2 - M}{M(M-1)} \tag{B.9}$$

Where,$Q_n \equiv \sum_{i=1}^{M} e^{in\phi_i}$, M is the number of particles considered and $P_{n,m} = n!/(n-m)!$ and the prime in the sum Σ' means that all indices in the sum must be taken different. The second step involves averaging over all events.

$$\langle\langle 2\rangle\rangle \equiv \left\langle\left\langle e^{in(\phi_1-\phi_2\rangle}\right\rangle\right\rangle \equiv \frac{\sum_{\text{events}} \left(W_{\langle 2\rangle}\right)_i \langle 2\rangle_i}{\sum_{\text{events}} \left(W_{\langle 2\rangle}\right)_i} \tag{B.10}$$

Where, $W_{\langle 2\rangle} \equiv M(M-1)$. The 2-particle correlator can be written as:

$$c_n\{2\} = \langle\langle 2\rangle\rangle \tag{B.11}$$

and, the v_n can be obtained directly as [44][45]:

$$v_n\{2\} = \sqrt{c_n\{2\}} \tag{B.12}$$

B.4 Results

B.4.1 v_2, v_3 vs Centrality

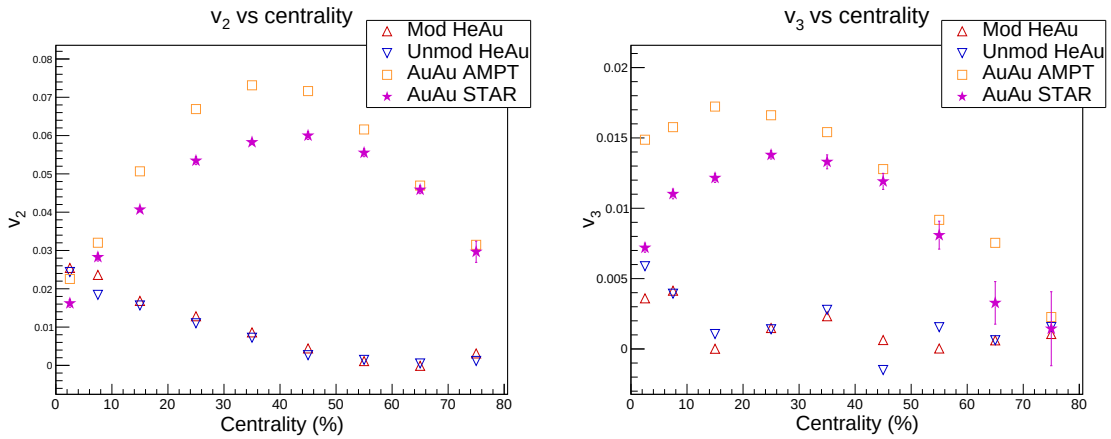

Figure B.6: (Left) v_2 vs centrality (Right) v_3 vs centrality. Open markers represent AMPT calculations, closed marker represents Au+Au 200 GeV STAR data.

Modified and Unmodified ^{3}He cases donot show much difference.

B.4.2 v_2, v_3 vs p_T

We have plotted $v_{2,3}$ vs p_T in three different centrality bins:

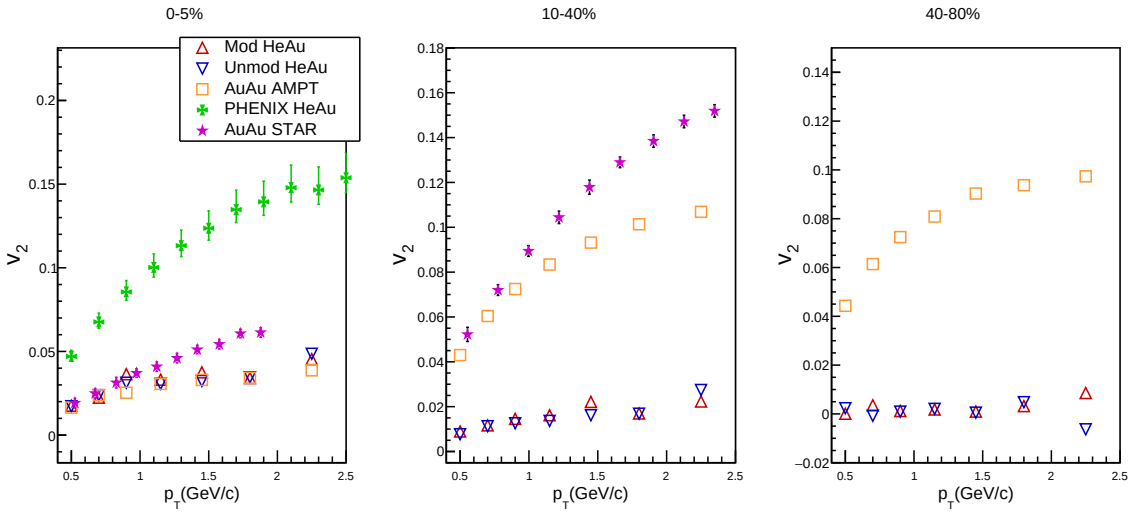

Figure B.7: Modified and Unmodified ^{3}He-Au AMPT show similar v_2 vs p_T trends. Our implementation of Au-Au AMPT explains the data till 1 GeV/c in 0-5% and 10-40% after which it underpredicts. ^{3}He-Au and AuAu AMPT show similar trends in 0-5% centrality. Both ^{3}He-Au AMPT underpredicts the data at 0-5% [43]

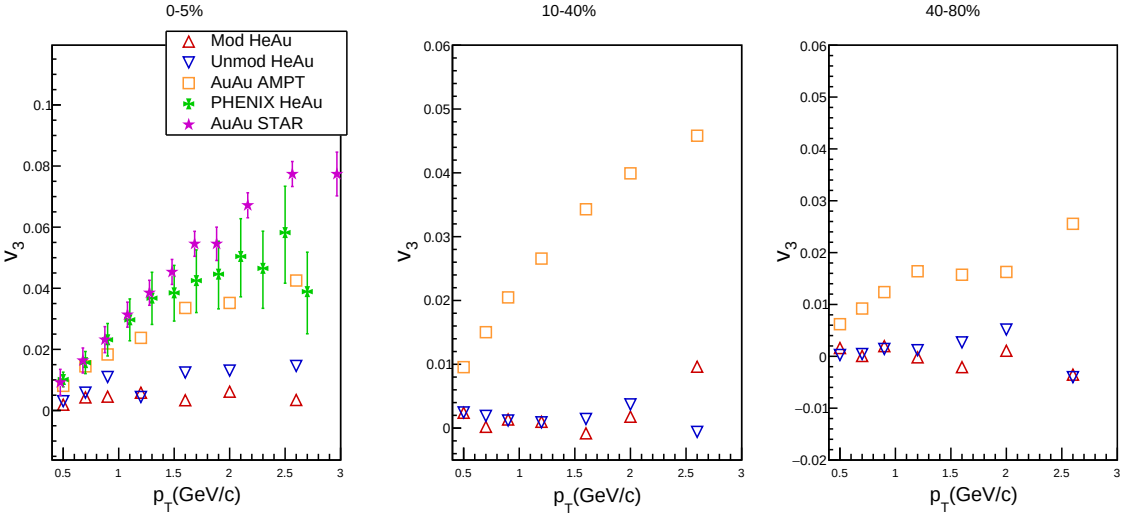

Figure B.8: Modified ^{3}He-Au gives lower v_3 than the Unmodified one in 0-5% centralitiy. Both underpredicts the PHENIX ^{3}He-Au data. [43]

B.4.3 v_2, v_3 vs η

We have plotted $v_{2,3}$ vs η in three different centrality bins:

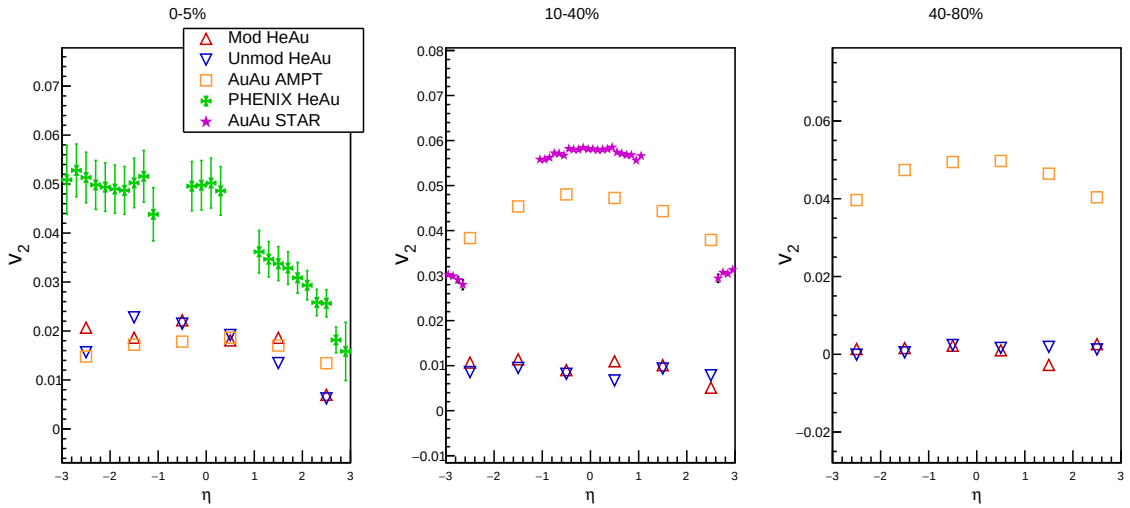

Figure B.9: Modified, Unmodified ^{3}He-Au AMPT and Au-Au AMPT show similar v_2 vs η trends at 0-5% centrality. At higher centralities, Au-Au v_2 is higher than both He3-Au implementations. In 0-5% centrality, both ^{3}He-Au AMPT implementations underpredict the PHENIX He3-Au data.[42]

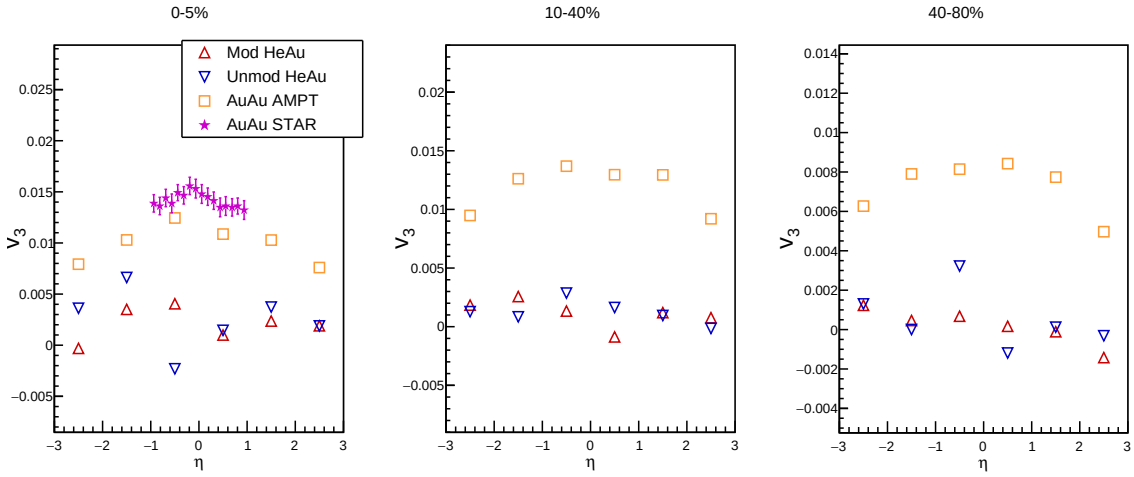

Figure B.10: Modified, Unmodified ^{3}He-Au AMPT show no particular trends and are lower than Au-Au AMPT in all centralities. Our Au-Au implementation compare well with data at in 0-5% centrality.

B.5 Summary and outlook

Pearson coefficient, $\epsilon_{2,3}$ vs. N_{ch} show some differences between the Modified and Unmodified ^{3}He nuclear profiles. As next step in this analysis, one can look at higher order correlators and correlation between different orders of anisotropic flow (Symmetric cumulants). Symmetric cumulants are calculated as [41],

$$\mathrm{sc}(n,m) \equiv \frac{\langle v_n^2 v_m^2 \rangle - \langle v_n^2 \rangle \langle v_m^2 \rangle}{\langle v_n^2 \rangle \langle v_m^2 \rangle} \tag{B.13}$$

References

[1] S. L. Glashow, Nucl. Phys. 22, 579 (1961); A. Salam and J. C. Ward, *Phys. Lett.* 13, 168 (1964); S. Weinberg, *Phys. Rev. Lett.* 19, 1264 (1967).

[2] https://en.wikipedia.org/wiki/Elementary_particle

[3] G. Dissertori, [Hep-Ex], *arXiv:1506.05407*, (2015).

[4] D. Gross and F. Wilczek, *Phys. Rev. Lett.* 30, 1343 (1973); *Phys. Rev D* 8, 3633 (1973).

[5] G. Baym, *Nucl. Phys. A* 698, XXIII (2002).

[6] J. Adams *et al.* (STAR Collaboration), *Nucl. Phys. A* 757,102 (2005).

[7] Z. Fodor, *Nucl. Phys. A* 715, 319 (2003).

[8] B. Mohanty, *New Journal of Physics* 13, 065031 (2011).

[9] R. V. Gavai and S. Gupta, *Phys. Rev. D* 71, 114014 (2005).

[10] Introduction to High Energy Heavy Ion Collisions by C. Y. Wong, World Scientific, Singapore, 1994.

[11] Md. Nasim, Ph.D. thesis, HBNI, 2014.

[12] https://www.star.bnl.gov/

[13] B. Bonner et al., *Nucl. Inst. and Meth. A* 508, 181 (2003).

[14] W.J. Llope et al., *Nucl. Inst. and Meth. A* 522, 252 (2005).

[15] E. C. Zeballos et al., *Nucl. Inst. and Meth. A* 374, 132 (1996).

[16] H. Bichsel, *Nucl. Instr. Meth. A* 562, 154, (2006).

[17] Particle Data Group.

[18] B. S. Pudliner, V. R. Pandharipande, J. Carlson, Steven C. Pieper, and R. B. Wiringa, *Phys. Rev. C* 56, 1720

[19] *Rev. Mod. Phys.*, Vol. 70, No. 3, July 1998.

[20] R. B. Wiringa, V. G. J. Stoks, and R. Schiavilla, *Phys. Rev. C* 51, 38 1995.

[21] J. Carlson, V. R. Pandharipande, and R. B. Wiringa, *Nucl. Phys. A*401, 59 1983.

[22] B.Alver, M.Baker, C.Loizides, P.Steinberg, *arXiv:0805.4411.*

[23] C. Loizides, J. Nagle, P. Steinberg, *arXiv:1408.2549.*

[24] ALICE-PUBLIC-2018-011, https://cds.cern.ch/record/2636623?ln=en

[25] ALICE Collaboration, K. Aamodt *et al. Eur. Phys. J. C* 65 (2010) 111125.

[26] ALICE Collaboration, K. Aamodt *et al. Eur. Phys. J. C* 68 (2010) 89108.

[27] D. Kharzeev, E. Levin, and M. Nardi, *Nucl. Phys. A*747 (2005) 609629, arXiv:hep-ph/0408050

[28] L. Adamczyk *et al.* (STAR Collaboration), *Phys. Rev. C* 96, 044904 (2017).

[29] B. I. Abelev *et al.* (STAR Collaboration), *Phys. Rev. C* 79, 034909 (2009).

[30] B. Abelev *et al.* (STAR Collaboration), *Phys. Rev. C* 81, 024911 (2010).

[31] X.-N. Wang and M. Gyulassy, *Phys. Rev. D* 44, 3501 (1991).

[32] H. Long, Ph.D. thesis, UCLA, 2002.

[33] V. Fine and P. Nevski, *Proc. CHEP* 2000, 143 (2000).

[34] L. Adamczyk et al. (STAR Collaboration), *Phys. Rev. C* 96, 044904 (2017).

[35] M. Shao, O. Barannikova, X. Dong, Y. Fisyak, L. Ruan *et al.*, *Nucl. Instr. Meth. A* 558, 419 (2006).

[36] D. Teaney, J. Lauret, and E.V. Shuryak, *Phys. Rev. Lett.* 86, 4783 (2001).

[37] U. Heinz and P. Kolb, *Nucl. Phys. A*702, 269 (2002).

[38] https://en.wikipedia.org/wiki/Pearson_correlation_coefficient

[39] B. Alver and G. Roland, *Phys. Rev. C* 81, 054905 (2010).

[40] A. M. Poskanzer and S. A. Voloshin, *Phys. Rev. C* no. CS6346.

[41] Md. Nasim, *Phys. Rev. C* 95, 034905 (2017).

[42] *arXiv:1807.11928v2*

[43] *arXiv:1507.06273v2*

[44] A. Bilandzic, R. Snellings, and S. Voloshin, *Phys. Rev. C* 83, 044913.

[45] A. Bilandzic, Anisotropic Flow Measurements in ALICE at the Large Hadron Collider, PhD thesis, Utrecht University, 2012.

[46] Z.W. Lin, C. M. Ko, B. A. Li, B. Zhang, and S. Pal *Phys. Rev. C* 72, 064901 (2005).